List of Publications:

1. **Jirwankar Y** and Dighe V. Identification and validation of Sertoli cell homing peptides as molecular steering for testis targeted drug delivery. Journal of Drug Targeting, 2023. https://doi.org/10.1080/1061186x.2022.2164007

2. Bhide AR, Suri M, Katnoria S, Kaur S, **Jirwankar YB**, Dighe VD, Jindal AB. Evaluation of Pharmacokinetics, Biodistribution, and Antimalarial Efficacy of Artemether-Loaded Polymeric Nanorods. Molecular Pharmaceutics, 2023. https://doi.org/10.1021/acs.molpharmaceut.2c00507

3. Mehta S, Bongcaron V, Nguyen TK, **Jirwanka Y**, Maluenda A, Walsh APG, Palasubramaniam J, Hulett MD, Srivastava R, Bobik A, Wang X, Peter K. An Ultrasound-Responsive Theranostic Cyclodextrin-Loaded Nanoparticle for Multimodal Imaging and Therapy for Atherosclerosis. Small 2022. https://doi.org/10.1002/smll.202200967

4. Surve DH, **Jirwankar YB**, Dighe VD, Jindal AB. Long-Acting Efavirenz and HIV-1 Fusion Inhibitor Peptide Co-loaded Polymer-Lipid Hybrid Nanoparticles: Statistical Optimization, Cellular Uptake, and In Vivo Biodistribution. Molecular Pharmaceutics, 2020. https://doi.org/10.1021/acs.molpharmaceut.0c00773

5. **Yugandhara Jirwankar**, Akanksha Nair, and Vikas Dighe, Phage display identified Leydig cell homing peptides **(Manuscript under preparation final stage)**

6. Mangesh Sane, **Yugandhara Jirwankar**, Sharad Bhagat, Sandip Sabale, Vikas Dighe, Vandana Patravale, Toxicological evaluation and application of new cationic lipid in developing sirolimus loaded cationic lipid-polymer hybrid nanoparticles. **(Manuscript under preparation final stage)**

Identification and validation of Sertoli cell homing peptides as molecular steering for testis targeted drug delivery

Yugandhara Jirwankar & Vikas Dighe

Taylor & Francis
Taylor & Francis Group

Check for updates

ORIGINAL ARTICLE

Identification and validation of Sertoli cell homing peptides as molecular steering for testis targeted drug delivery

Yugandhara Jirwankar [ID] and Vikas Dighe [ID]

National Centre for Preclinical Reproductive and Genetic Toxicology, ICMR – National Institute for Research in Reproductive and Child Health, Mumbai, India

ABSTRACT

The testicle, an organ privileged with immunity because of Blood-Testis Barrier (BTB), poses a major impediment to developing and delivering drugs to the testes. These problems can be prevented by targeting testicular cells using specific ligands, such as homing peptides. This is the first study to demonstrate the successful selection of Sertoli cell homing peptides using a phage display peptide library. The identification of peptides is performed with Sanger sequencing and high-throughput NGS. The Sertoli cell and testis targeting potential of the SCHP1 and SCHP2 was confirmed using confocal microscopy and flow cytometry of the FITC-labelled peptides and *in vivo* bio-distribution of the corresponding Cy5.5-tagged peptides. Secondary structures were predicted in the setting of different polarity by circular dichroism. The results suggest that SCHP1 and SCHP2 can effectively target Sertoli cells. *In vivo* bio-distribution in mouse models indicated significantly higher uptake of SCHP1 and SCHP2 by testes compared with the heart, brain, and spleen. SCHP1 and SCHP2 can be adopted as molecular steering for targeted male contraceptive delivery, treatment of testicular cancer, and male infertility. Further development of the peptides into peptidomimetics may increase their stability, and information on the molecular targets of these peptides may reveal their therapeutic potential.

Introduction

Germ cells, Sertoli cells, and Leydig cells are important components of the testis. Sperm production occurs in seminiferous tubules with the help of Sertoli cells, and androgen production occurs between seminiferous tubules by Leydig cells. Various disorders are associated with these testicular cells, including infertility, testicular cancer, and oxidative stress. Male factor infertility accounts for nearly 40% of 8-10% of infertile couples worldwide and 3.9-16.8% in India.[1] Male infertility could be because of various reasons, including endocrine, iatrogenic, congenital abnormalities, acquired testicular damage, varicocele, oxidative stress, male accessory gland infection, genetic or idiopathic [1]. Current management strategies for male factor infertility include drug treatment, depending on the cause of infertility and artificial reproductive technologies. Drug treatment includes hormonal treatment, antioxidant treatment, and a combination of both [2, 3]. Systemic delivery of exogenous testosterone to treat male infertility result in feedback inhibition, ultimately worsening the condition [4]. Testicular cancer accounts for 1% of all men globally, but it is the most common malignancy between the age group of 15 to 35 [5]. Germ cell cancer accounts for approximately 90 to 95% of testicular cancers [6]. Current treatment strategies include orchiectomy, active surveillance radiotherapy, chemotherapy, and RPLND-Retroperitoneal Lymph node dissection [7, 8]. Chemotherapy plays a significant role in the treatment of germ cell tumours with an approximate 95% cure rate, but there are various complications, such as systemic toxicities, cardiovascular effects, and secondary malignancies. These treatment-related toxicities could be acute or chronic with long-term effects [9]. The people are now accepting the active role of a male partner in family planning, but male contraceptives are limited to condoms and vasectomy. Vasectomy is non-reversible, and condoms have marginal efficacy [10]. Testosterone has been used as a reversible male contraceptive that acts *via* a negative feedback mechanism, but being a hormone, it affects the normal sexual functions of the individual. Researchers are now focussing on non-hormonal instead of hormonal contraceptives because it will not affect testosterone concentration and normal sexual functions of the individual. A few examples of non-hormonal contraceptives include adjudin, H2-Gamendazole, eppine-based drugs etc. [11]. In recent years, developments have been made in non-hormonal contraceptive drugs such as adjudin, but the delivery of this drug faces the same problems, such as a meagre margin between safety and efficacy [12].

Conventional treatment and delivery methods of drugs for testicular disorders face limitations such as low efficacy because of the need for high doses and high dosing frequency, systemic toxicities, the problem of feedback inhibition, etc. All these issues can be solved with the help of selective targeting of drugs to the testis. Drug targeting to testis to treat testicular pathologies will be more advantageous than conventional drug delivery methods. Targeted drug delivery assists the drug molecules in accumulating at the desired site or tissue and reduces the systemic side effects. Passive targeting is based on anatomic or physiological factors and active targeting utilises the targeting ligands for the delivery of the drugs [13]. Depending upon the type of receptor expressed or overexpressed, the location and nature of the cell, and the metabolism

profile of a particular cell or pathological condition, they have specific tags called zip codes [14]. These zip codes can be exploited to differentiate between target and non-target tissues or cells for identifying targeting ligands. Peptides have shown promising properties as ligands. They have various advantages over other ligands, such as high specificity, low immunogenicity, ease of modification, low cost, rapid clearance from non-target sites. [15]. Phage display peptide libraries provide an excellent platform for selecting such peptide ligands using the procedure called bio-panning. The technique was first described by George P. Smith in 1985, in which a DNA encoding for a specific peptide sequence is incorporated into the bacteriophage genome, leading to the expression of the peptide on the bacteriophage coat [16]. People have identified peptide ligands targeting various cancers and normal organs, including the brain, kidney, skin, pancreas, prostate, breast tissue, human umbilical cords, adipose tissue, and heart [14, 17–25]. RGD and NGR peptides recognising integrin and aminopeptidase N are the tumour-targeting peptides. Peptides identified using a phage display libraries are being practiced to deliver drugs across blood tissue barriers, such as the blood-brain barrier and gastrointestinal tract [26]. Homing peptides are highly selective and potent hence provide good efficacy, safety, and tolerability. They are cost-effective and easy to manufacture and modify [27]. Novel peptides targeting Sertoli cells can open new avenues for targeted drug delivery to the testis to deal with various testicular pathologies.

Targeting testicular cells and tissue is important to overcome the hurdle the Blood-Testis Barrier (BTB) provides in developing and delivering drugs to treat testicular anomalies. Almost every testicular pathology or contraceptive drug is cell-specific or targets cell-specific molecules, but there is no testicular cells targeting ligand available to date. Somatic cells like Sertoli and Leydig cells, and also the germ cells can be targeted for treating or delivering drugs for specific testicular pathologies [28]. Sertoli cells form the blood-testis barrier, and the process of spermatogenesis occurs in the compartment protected by this barrier; hence, Sertoli cells provide the potential target for the development and delivery of male contraceptive drugs [29]. Antioxidants such as superoxide dismutase targeting to Sertoli cells can help to address the problem of intratesticular oxidative stress [28, 30]. Ligands selectively targeting Sertoli cells may open new avenues for treating various testicular disorders. In this study, we have attempted to identify Sertoli cell homing peptides for testicular targeting using a phage display peptide library. The Sertoli cell homing peptides (SCHPs) may provide better opportunities in the future for the targeted delivery of drugs and male contraceptives to the testis.

Materials and methods

Phage display library

Ph.D.-12, a combinatorial phage display library of random 12-mer peptides fused to a minor coat protein (pIII) of the M13 phage, was purchased from New England Biolabs. The displayed peptide is expressed at the N-terminus of pIII. The library consists of approximately 10^9 unique sequences. 10 µL of the library was used to start the experiment, which contained approximately 100 copies of each peptide.

Cell culture

TM4 (Mouse Sertoli cells) (ATCC CRL 1715) were obtained from an American-type culture collection, and Dr. Susan Thomas of Bioinformatics Centre ICMR-NIRRCH gifted HEK293. TM4 cells were cultured in DMEM (Dulbecco's Modified Eagle Medium) Nutrient Mixture F-12 supplemented with 5% horse serum and 2.5% foetal bovine serum, and HEK293 cells were cultured in DMEM Nutrient Mixture F-12 (Ham) (1:1) supplemented with 10% foetal bovine serum. Both the cell lines were maintained at 37° C with 5% CO2.

Animal use and care in the study

All the procedures performed on adult Balb/C male mice (6-8 weeks old) were approved by the Institutional Animal Ethics Committee of ICMR-National Institute for Research in Reproductive and Child Health Mumbai (IAEC-03/20).

In-vitro biopanning

Mouse Sertoli cells (TM4) were seeded at the density of 0.5 x 10^6 cells/well in 6 well plate before 48 h of biopanning. The spent medium was removed on the day of biopanning, and DMEM/F12 w/o serum was added to the wells. After 1 h incubation at 37 °C with 5% CO2, biopanning solution containing 1*10^{11} phages 10 µL of PhD-12 library, protease inhibitor, and chloroquine in PBS (Phosphate Buffered Saline) with 0.1% BSA (Bovine Serum Albumin) was added and incubated for 1 h. Unbound phages were removed by washing four times for 5 min each with 0.1% BSA in PBS. The cell surface homing phages were eluted with two washes of 1 ml of 0.1 M HCl-Glycine, pH 2.2 + 0.9% NaCl for 5 min. Again, the cells were washed with 0.1% BSA in PBS twice, and 1 ml of 30 mM Tris–HCl, pH 8.0, was added and incubated on ice for 30 min, and cells were frozen at −20° C overnight. The next day, cell-penetrating phages were collected from the disrupted cells. Enrichment of the Sertoli cell surface homing and Sertoli cell-penetrating phages was achieved with three rounds of biopanning [31].

In-vivo biopanning

Amplified Sertoli cell surface homing phage pool and Sertoli cell-penetrating phage pool from the 3rd round of in-vitro biopanning were used to perform in-vivo biopanning. Briefly, 1*10^{11} Phages in 100 µL of DMEM medium were injected into Balb/C mice intravenously and allowed to circulate for 30 min. Mice were sacrificed, and all vital organs were collected and stored at −80 °C. The next day, testis was minced in DMEM medium, and phages were recovered and amplified for the next round of biopanning. Enrichment of testis homing phages was achieved through three rounds of such in-vivo biopanning [32].

Phage titration and amplification during biopanning

Phage titration was performed with the qPCR standard curve method as described earlier by Peng et al. [33], tenfold concentrations of M13 ssDNA from 0.1 fg/µL to 10^6 fg/µL (2.689*10^1 gc/µL to 2.689*10^8 gc/µL) were used as standards. Samples were precipitated with PEG (Polyethelene glycol)/NaCl for M13 phage isolation and treated with DNase I at 37 °C for 10 min, followed by heat denaturation at 100 °C; these samples were used as a template for qPCR. The reaction mixture of 10 µL consists of 5 µL SYBr green Power Up 2x MM, 0.5 µL (10 µM stock) forward primer and reverse primer each, 2 µL nuclease-free water, and 2 µL template ssDNA (standard/sample). Primers used are forward primer 5'-CAC CGT TCA TCT GTC CTC TTT-3' and reverse primer 5'-CGA CCT GCT CCA TGT TAC TTA G-3'. Reaction conditions were 50 °C for 2 min, 95 °C for 2 min, 40 cycles of 95 °C for 15 s and 60 °C for

1 min, melt curve at 95 °C for 15 s, 60 °C for 1 min, and 95 °C for 15 s. The reaction was performed on Applied Biosystems's QuantStudio5 Real-time PCR and analysed with QuantStudio™ Design and Analysis software.

Plaque assay and Sanger sequencing

Plaque assay was performed according to the New England Biolab's instruction manual. Blue-colored plaques were picked and amplified in E. coli ER2738 host cells. Amplified phage clones were isolated with PEG/NaCl precipitation, and ssDNA was isolated according to the protocol mentioned by Green et al. [34]. PCR was performed to amplify the product using forward primer: 5'-TGG TTG TTG TCA TTG TCG GC-3' and reverse primer: 5'-GCA AGC CCA ATA GGA ACC CA-3'. PCR reaction mixture of 50 μL consisted of 25 μL 2x DreamTaq Green PCR Master Mix, 2.5 μL each of forward and reverse primer (10 μM stock), 15 μL nuclease-free water, and 5 μL template. PCR conditions were initial denaturation at 95 °C for 5 min, 40 cycles of denaturation at 95 °C for 30 s, annealing at 55 °C for 30 s, extension at 72 °C for 30 s, and Final extension at 72 °C for 5 min. The reaction was performed on Agilent's Sure Cycler 8800. The PCR product was run on 1.8% agarose gel, extracted using PureLink Quick gel extraction kit; Sanger sequencing was performed with -96gIII reverse sequencing primer provided in the PhD-12 phage library kit.

Next-generation sequencing of phage pool

Phage pool from the 3rd round (last round of in-vitro panning) and the 6th round (last round of in-vivo panning) were subjected to NGS. Phage DNA (ssDNA) was isolated from the phage pools as described by Green et al. [34], and PCR was performed to prepare 77 bp amplicon (Supplementary Figure 2) for Illumina sequencing; the primers and barcodes used were picked from Matochko et al. [35], forward primer 5'CCT TTC TAT TCT CAC TCT3', reverse primer 1 with barcode 5'TTC CGA TAA CCC GAA CCT CCA CC3' and reverse primer 2 with barcode 5'CTG ACC GAA CCC GAA CCT CCA CC3'. The reaction mixture consisted of 25 μL OneTaq® Hot Start Quick-Load® 2X Master Mix, 5 μL of each forward and reverse primer, and 5 μL of template ssDNA. The reaction was performed at 95 °C for 3 min, 35 cycles of denaturation at 94 °C for 10 s, annealing at 60 °C for 20 s, elongation at 72 °C for 30 s, and final elongation at 72 °C for 5 min. The PCR product was run on 2% agarose gel and was extracted using GeneJet gel extraction kit. Polyacrylamide gel electrophoresis (10%) was performed with 2 μL of the final product long with low range DNA ladder. The final 77 bp PCR product was further submitted for Illumina sequencing at Bioxplore labs, Chennai, India.

Peptide synthesis

Biological grade SCHP1 and SCHP2 peptides with >95% purity were commercially obtained from AsianBioChem, Thrissur, Kerala, India. SCHP1-Ahx-FITC, SCHP2-Ahx-FITC and {C(Cy5.5)}-SCHP1, {C(Cy5.5)}-SCHP2 with 99% purity were obtained from Lifetein, LLC, USA.

Confocal microscopy of M13 bacteriophage

The homing potential of the SCHP1 and SCHP2 phages to TM4 cells was analysed with an anti-M13 antibody. Briefly, 0.2*10^6 cells were seeded on pre-sterilized coverslips in 12-well plates and allowed to attach for 24 h. These cells were incubated with 1*10^11 SCHP1/SCHP2 phages for 1 h. After incubation, the cells were washed three times in DPBS w/Ca, Mg (Dulbecco's phosphate-buffered saline with calcium and magnesium), and fixed for 10 min with 4% paraformaldehyde at room temperature. Blocking was performed in 1% BSA for 1 hand incubated with an anti M13 antibody (Cat# MA1-06604) at 4 °C overnight. The next day, primary antibody was removed, cells were washed three times, 5 min each with DPBS, and a secondary antibody labelled with Alexa Fluor 594 was added for 1 h. After 1 h incubation, cells were washed three times with DPBS, and the coverslips were mounted on clean slides with vectasheild reagent and observed at NIRRCH core confocal microscopy facility.

Confocal microscopy of peptides

Briefly, 0.1*10^6 cells were seeded on a pre-sterilised coverslip in 12-well plates and allowed to attach overnight. The next day, FITC labelled SCHP1, SCHP2 were added per well and incubated for 1 h. Cells were washed three times with DPBS w/Ca Mg, fixed with 4% PFA (Paraformaldehyde), and counter-stained with DAPI for the nucleus and rhodamine-phalloidin (Invitrogen Cat#R415) for the cytoskeleton. Slides were prepared and analysed with confocal microscopy.

Flow cytometry analysis of peptides

Briefly, 0.5*10^6 cells were seeded per well in 6-well plates and allowed to attach overnight. The next day, cells were treated with different concentrations of the FITC labelled SCHP1 and SCHP2 for 1 h. After the incubation, cells were detached with 1 mM EDTA solution, washed three times with DPBS, and analysed with the flow cytometer.

MTT assay

Cytotoxicity of the SCHP1 and SCHP2 peptides was assessed with MTT assay. Briefly, 0.05*10^6 TM4 cells were seeded per well of 96-well plates and allowed to attach overnight. The next day, the cells were treated with two-fold increasing concentrations of SCHP1/SCHP2 peptides for 48 h. After 48 h incubation, the spent medium was removed, and MTT solution was added at 50 μg/well and incubated for 4 h at 37 °C. MTT solution was removed, and 100 μL of DMSO (Dimethyl sulfoxide) was added to each well and incubated for 30 min at room temperature. OD was taken at 570 nm, and the percent cell viability was calculated.

Circular dichroism spectroscopy

Circular dichroism (CD) spectroscopy was performed on a Jasco J-810 spectropolarimeter using a 1-mm cuvette. The peptides were dissolved in different concentrations, i.e. 10%, 25%, 50%, 75%, and 90% of trifluoroethanol (TFE) in water at a concentration of 0.5 mg/mL. Spectra were collected every 2 nm from 260 to 190 nm. The CD spectra are reported as Molar ellipticity.

Plasma stability study

SCHP1/SCHP2 unlabelled peptide, FITC labelled and Cy5.5 labelled was dissolved in 10 μL of DMSO followed by 1 ml of 25% mouse

plasma in DMEM medium. The mixture was incubated at 37oC and 100 μL of the mixture was taken at 0 min, 15 min, 30 min, 1 h, 2 h, 4 h, 6 hand 6 htime point. Plasma protein of the reaction mixture was precipitated with the addition of 200 μL of 95% chilled ethanol followed by vortex and centrifugation at 13000 g for 2 min at 4oC. The supernatant was collected and 60 μL of it was injected to C18 column to study the stability of the peptide over the period of 8 h. For the mobile phase of RP-HPLC, a mixture of water (0.1% TFA) and acetonitrile (0.1% TFA) in a linear gradient of 25-50%, 25-65% and 25-80% acetonitrile in 20 min was used for unlabelled, FITC labelled and Cy5.5 labelled peptides respectively. UV detection wavelengths were set at 220 nm, 541 nm, and 675 nm for unlabelled peptides, FITC labelled and Cy5.5 labelled peptides, respectively. Stable peptide percentage at different time point was determined by considering 0 min peptide concentration as 100% peptide, and the test was performed in triplicates.

In-vivo imaging

SCHP1 and SCHP2 conjugated to Cy5.5 NIR dye were obtained from LifeTein LLC for in vivo imaging using IVIS lumina III in-vivo imaging system. Adult male Balb/C mice (6-8 weeks old were randomly distributed in three groups (n = 9), i.e. SCHP1, SCHP2, and free Cy5.5 dye. Cy5.5 labelled SCHP1 and SCHP2 were injected into mice intravenously at 20 μg in 100 μL PBS. Mice were dissected, and vital organs, including testis, were collected after 1 h, 6 h, and 24 h. The organ imaging was performed using Perkin Elmer's IVIS lumina III small in-vivo imaging system, and images were analysed with Living Image software.

Results and discussion

Screening of Sertoli cell homing peptides

The PhD-12 phage display peptide library was used to screen the Sertoli cell homing peptides. Initially, in two separate sets of experiments, three rounds of bio-panning were performed on TM4 mouse Sertoli cells to get SCSHPs (Sertoli cell surface homing peptides) and SCPPs (Sertoli cell-penetrating peptides). The enriched SCSHP and SCPP phage pool obtained after the 3rd round of bio-panning with the TM4 cell line was used as input for two separate in-vivo bio-panning in a mouse model, and three rounds of in-vivo bio-panning were performed. After the 6th round of bio-panning, i.e. the 3rd round in the mouse model, we got enriched SCSHP and SCPP pools from the testis. M13 bacteriophage titration after each round indicated an enrichment of the phage pool in 3rd and 6th rounds of bio-panning for screening of SCSHPs and SCPPs (Figure 1A).

Identification of Sertoli cell homing peptides

Sertoli cell homing peptide identification was performed using Sanger sequencing and next-generation amplicon sequencing. A plaque assay was performed for the phage pool obtained after the 3rd and 6th rounds of bio-panning for screening of SCSHPs and SCPPs. PCR was done using M13 phage ssDNA as a template to amplify the product for Sanger sequencing. PCR products of 416 bp (Supplementary Figure 1) from 277 phage clones were subjected to Sanger sequencing; after removing sequences w/o 36 bp insert, 254 total peptide sequences were obtained, of which 137 were unique peptides (Supplementary Table 1). Depending

upon the frequency of the peptides in the SCSHP and SCPP phage pool, these were named SCHP1 to SCHP137, and the top 18 SCHPs were found more than once in either of the pool from 3rd or 6th rounds. The overall summary of the peptide obtained with Sanger sequencing is shown in Table 1.

Phage pools from the 3rd round (last round of in-vitro panning) and the 6th round (last round of in-vivo panning) from the SCSHP and SCPP biopanning were subjected to high throughput sequencing. The number of unique peptides normalised with a total number of good reads for both the SCSHP and SCPP panning experiments was decreased in the 6th round compared to the 3rd round (Figure 1B), which indicates enrichment of a few peptides from 3rd round to 6th round. In both the SCSHP and SCPP biopanning, only 14.90% and 20.91% peptides obtained from TM4 cells in the last in-vitro round were enriched in the testis and comprised 54.67% and 53.84% of the last rounds of in-vivo biopanning (Figure 2). The overall comparison of the unique peptides found in all four sequencing runs is shown in (Figure 2C). Only 1551 peptides were found common in all the four phage pools sequenced. Combined peptide frequency suggests that few top peptides with a count $>10^5$ dominated the selected phage pool from the 3rd and 6th rounds of both the biopanning experiments (Figure 1C and D). Only three top peptides were found with a count of $>10^5$ in the 6th round of both panning experiments. GSWNTFRAQPTI and YSLRLTSVTAPT are the topmost peptides in SCSHP and SCPP biopanning experiments, respectively, and TGSAKFLQRDTH is the on the 3rd position in both experiments (Figure 3). Peptides GSWNTFRAQPTI and YSLRLTSVTAPT were selected for further validation and named SCHP1 and SCHP2, respectively. The top 10 peptides from each of the phage pools sequenced are shown in Table 2. with their respective frequency. Biopanning Data Bank (BDB) [36] search was performed to know whether any of SCHP1 and SCHP2 were previously reported in the literature. SCHP1 was previously reported as a gallium-binding peptide [37], but SCHP2 was not reported anywhere in the literature. A peptide scan was done on SAROTUP [38], a suite of tools for finding potential target-unrelated peptides from phage display data, and we could not find any target-unrelated peptide motifs for both SCHP1 and SCHP2.

The positional abundance of amino acids

The positional amino acid abundance of common 1551 differed from the top 100 common peptides; again, it was different for aligned and non-aligned peptide sequences. In common, 1551 peptides Ser, Pro, Ala, Thr, Arg, and Lys were found to be enriched at the top position (Figure 4C). However, when aligned, Pro was found to be highly enriched at a specific position (Figure 4D). Non-aligned top 100 common sequences indicated an enrichment of Ser similar to top 1551 peptides, but other amino acids such as Ala, Pro, Arg, Thr, and Lys were enriched at a few positions (Figure 4A). Aligned top 100 common sequences showed the highest enrichment of Ser at a specific position, followed by Thr at two positions (Figure 4B).

Motif discovery and seqlogo

Motif discovery analysis of common 1551 peptide sequences using STREME (Sensitive, Thorough, Rapid, Enriched Motif Elicitation) [39] (https://doi.org/10.1093/bioinformatics/btab203) resulted in six enriched ungapped motifs with p-value <0.05. GSAK motif is enriched in 203 (13.1%) sequences followed by FRAQPTI, YSLRLT,
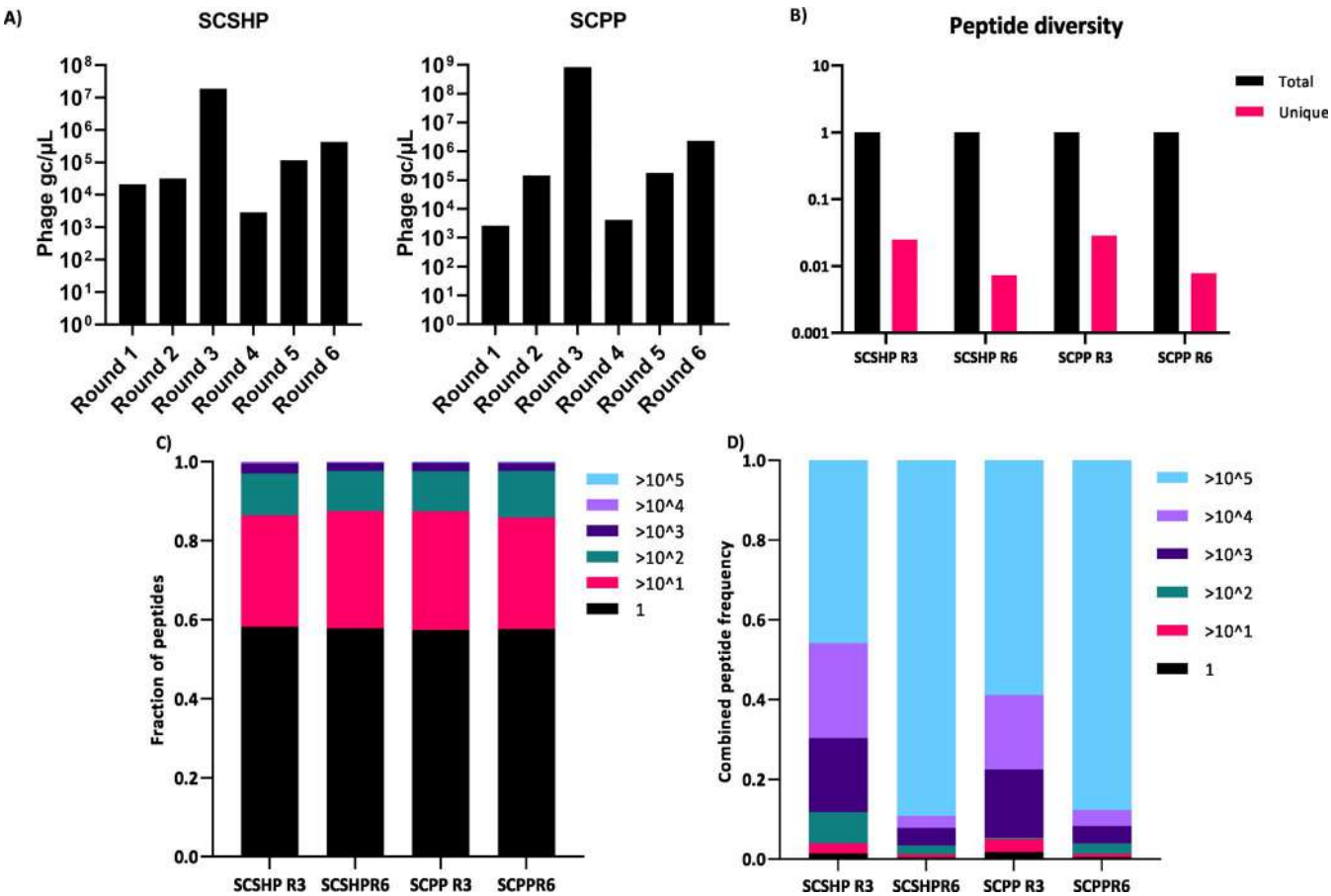
Figure 1. A. Phage titration after each round of SCSHP and SCPP biopanning experiments, B. normalised peptide diversity in each phage pool sequenced with Illumina NGS, i.e. SCSHP R3 and SCPP R3 (last round of *in-vitro* biopanning), SCSHP R6 and SCPP R6 (last round of *in-vivo* biopanning), C. Fraction of the peptides with respective peptides frequency in 3rd and 6th round of SCSHP and SCPP biopanning phage pools sequenced with Illumina NGS. D. Combined peptide frequency of the all peptides in 3rd and 6th round of SCSHP and SCPP biopanning phage pools sequenced with Illumina NGS.

Table 1. Summary of phage clones subjected Sanger sequencing.

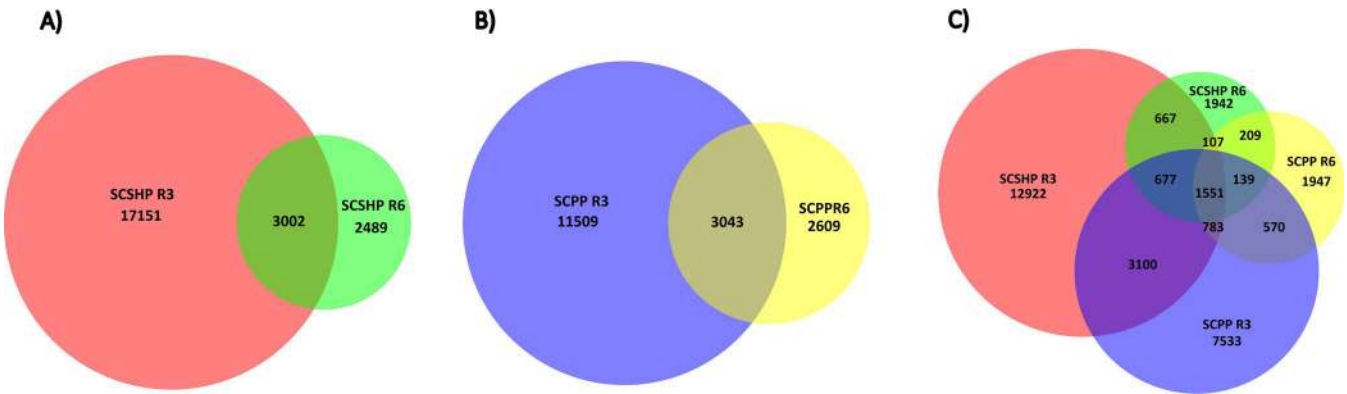|	SCSHP R3	SCSHP R6	SCPP R3	SCPP R6
No. of phage DNA sequenced	95	38	96	48
Empty/ mixed 36 bp DNA phage	6	7	7	3
No. peptide sequences obtained	89	31	89	45
Unique peptides	80	17	52	3
Total peptides			254	

Figure 2. *Venn* diagram showing common peptides obtained in the phage pool of round 3 and round 6 of SCSHP (A), common peptides obtained in the phage pool of round 3 and round 6 of SCPP (B), and comparisons between all four phage pools sequenced (C).
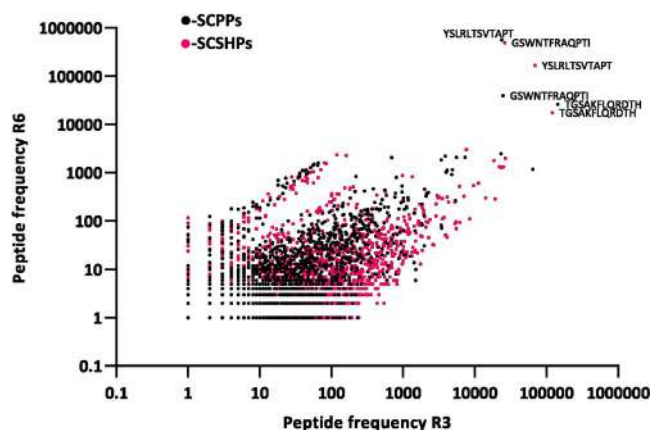
Figure 3. Scatter plot of 1551 peptides common in SCSHP and SCPP and their frequency in round 3 and round 6 of each biopanning experiment showing sequences of top three peptides.

SVTAPT, RDTH, and MKA (Figure 5 A–F), a summary of their p-values, E-values, and sites are shown in Supplementary Table 2. Further, these motifs were submitted to Tomtom, a motif comparison tool (https://doi.org/10.1186/gb-2007-8-2-r24) [40] which compared the submitted protein motif with motifs on the prosite database. Out of six enriched motifs, only GSAK and YSLRLT resulted in one hit each with E value <0.1. The motif similarity of GSAK and YSLRLT was found with Eukaryotic initiation factor 5A hypusine signature (PS00302) and Stress-induced proteins SRP1/TIP1 family signature (PS00724), respectively (Supplementary Figure 3). Though the E-value for these two alignments is <0.1, these motifs are not 100% similar to their hits, indicating the novelty of the discovered motifs. Seqlogo analysis of common 1551 peptides with TBtool (Figure 5G) revealed GSWNTFRAQ and PTI as enriched domains, which is the actual sequence of the SCHP1 peptide.

Table 2. Top 10 peptides from all four phage pools subjected to Illumina NGS.

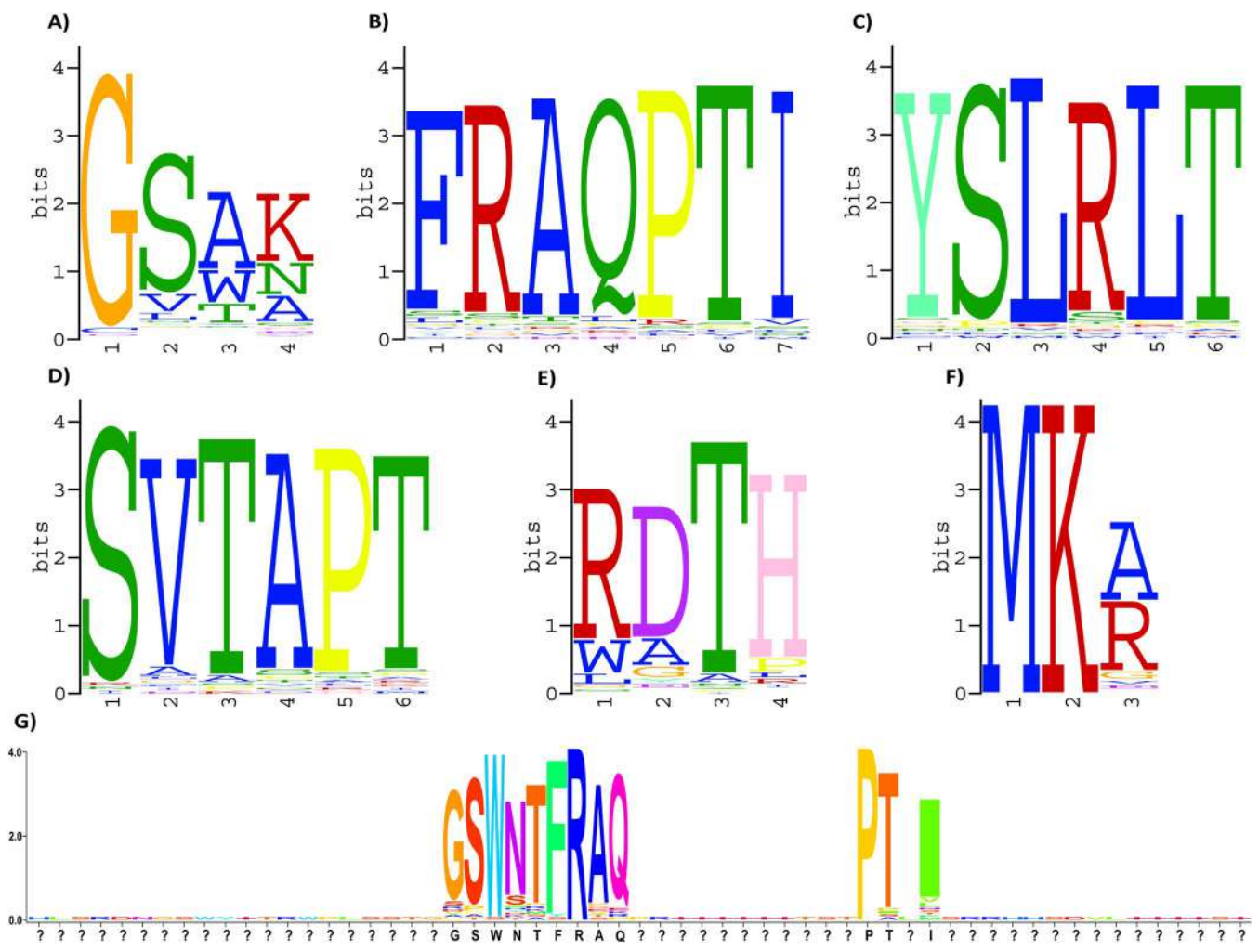| Protein sequence	R3 SCSHP frequency % peptide frequency	Protein sequence	R6 SCSHP frequency % peptide frequency	Protein sequence	R3 SCPP frequency % peptide frequency	Protein sequence	R6 SCPP frequency % peptide frequency
TGSAKFLQRDTH	119965 (14.67%)	GSWNTFRAQPTI	493948 (64.97%)	TGSAKFLQRDTH	143455 (27.81%)	YSLRLTSVTAPT	570722 (78.71%)
YSLRLTSVTAPT	68959 (8.44%)	YSLRLTSVTAPT	¹66731 (21.93%)	TSWPWFQSNPPR	64484 (12.50%)	GSWNTFRAQPTI	39328 (5.42%)
MKAHHSQLYPRH	26494 (3.24%)	TGSAKFLQRDTH	17482 (2.30%)	GSWNTFRAQPTI	24557 (4.76%)	TGSAKFLQRDTH	26055 (3.59%)
GSWNTFRAQPTI	25921 (3.17%)	MGHSVSAVPP*T	3024 (0.40%)	YSLRLTSVTAPT	23668 (4.59%)	MGHSVSAVPP*T	2493 (0.34%)
WGVTKPIRTSTL	25006 (3.06%)	GSWNTLRAQPTI	2329 (0.31%)	MGHSVSAVPP*T	23192 (4.50%)	SPWATHPVSMKR	2201 (0.30%)
SPWATHPVSMKR	23530 (2.88%)	GPWNTFRAQPTI	2256 (0.30%)	MKAHHSQLYPRH	7293 (1.41%)	MKAHHSQLYPRH	2088 (0.29%)
ARSLEPAPSRHS	22042 (2.70%)	MKAHHSQLYPRH	1985 (0.26%)	GSAARTISPSLL	5540 (1.07%)	GSAARTISPSLL	2077 (0.29%)
TLGLRPVPVATT	19228 (2.35%)	GSAARTISPSLL	1787 (0.24%)	GSKYPSLHDRVR	5363 (1.04%)	SLVTRVPSPDFL	2054 (0.28%)
GSAARTISPSLL	18421 (2.25%)	GSRNTFRAQPTI	1596 (0.21%)	AGVYPHRLSDVL	4871 (0.94%)	ARSLEPAPSRHS	1836 (0.25%)
TPTNQGGQARGM	14106 (1.73)	GSWSTFRAQPTI	1559 (0.21)	TLGLRPVPVATT	4726 (0.92)	YPLRLTSVTAPT	1588 (0.22)
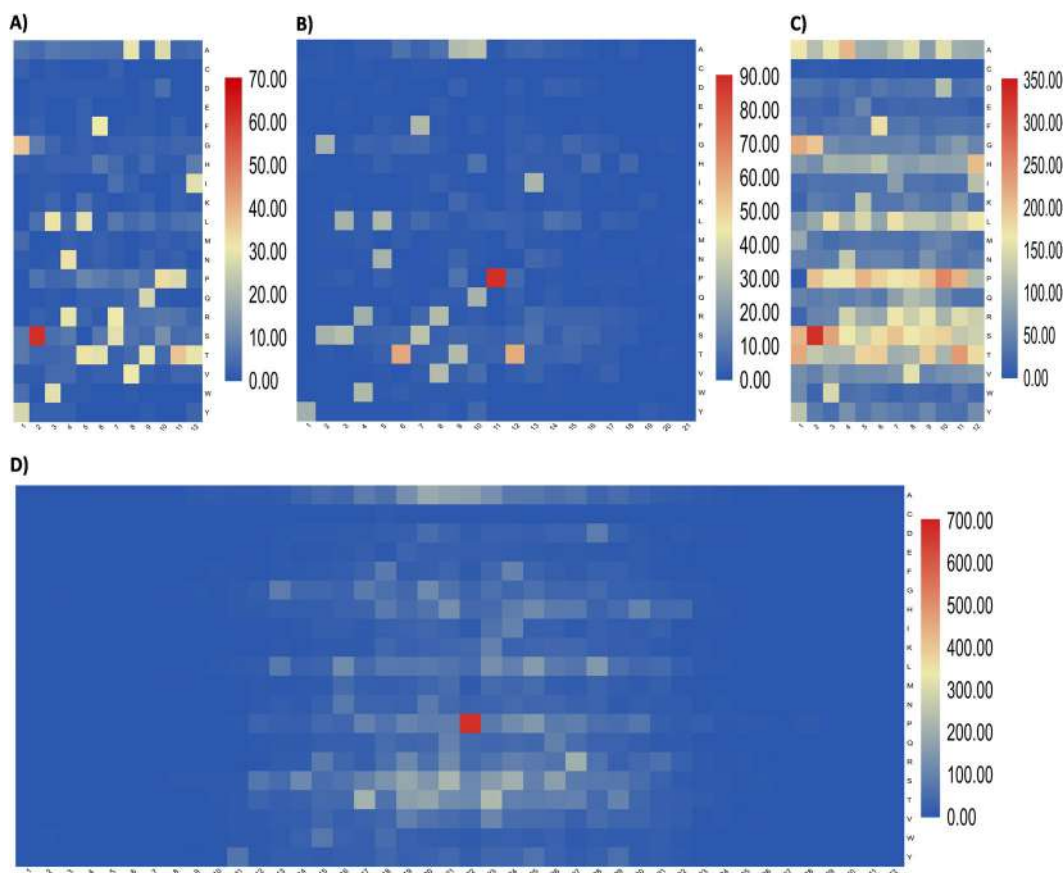
Figure 4. Heat maps of summary of the positional amino acid abundance of top 100 common peptides non-aligned (A), aligned (B) and common 1551 peptides non-aligned (C), aligned (D). Positional amino acid abundance was calculated with BioEdit software, and heat maps were generated using TB tools.

Figure 5. Motif discovered from 1551 common peptides with p-value > 0.05. A. GSAK, B. FRAQPTI, C. YSLRLT, D. SVTAPT, E. RDTH and F. MKA. Motif discovery analysis was performed using the STREME motif discovery tool on the MEME suite [39]. G. Sequence logo of common 1551 peptides generated through TBtools.

Homing of SCHP1 and SCHP2 phage to TM4 mouse Sertoli cells

M13 bacteriophages displaying SCHP1/SCHP2 peptides were amplified in E. coli ER2738, and the sequence was confirmed with Sanger sequencing. SCHP1/SCHP2 phages were incubated for 1 h with the TM4 cells, and then the cells were fixed with 4% paraformaldehyde. The homing potential of the SCHP1/SCHP2 phages was checked with anti M13 antibody and detected with Alexa Fluor 594 labelled secondary antibody. Empty phage (w/o 36 bp insert) was used as a control. Confocal image analysis of these cells showed the internalisation of SCHP1 and SSCHP2, displaying phages but not empty phages (Figure 6). This confirmed the homing potential of the SCHP1 and SCHP2 phages to TM4 cells.

Specific homing of SCHP1 and SCHP2 peptides to TM4 mouse Sertoli cells

Uptake of FITC-Ahx-SCHP1 and FITC-Ahx-SCHP1 by TM4 and HEK293 cells were studied with confocal microscopy and quantitatively by flow cytometry. Confocal micrographs of the TM4 and HEK293 show that the peptides SCHP1 and SCHP2 can bind to TM4 cells but not HEK293 cells (Figure 7A and B). SCHP1 and SCHP2 uptake by Human Coronary Artery Smooth Muscles Cells (HCASMCs) is also lower compared with TM4 cells (Supplementary Figure 4A), and of
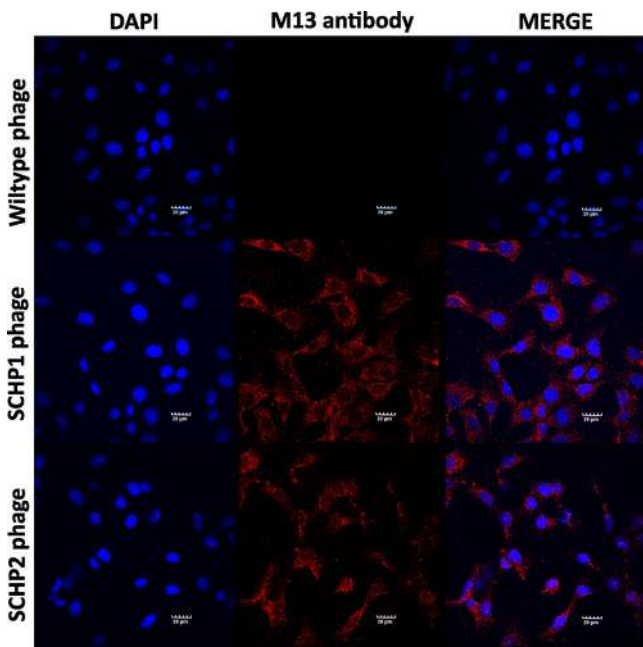

Figure 6. Confocal micrographs of TM4 cells treated with wild-type phage, SCHP1, and SCHP2 phage were detected with anti-M13 antibody labelled with Alexa Fluor 594 and counter stained with DAPI.
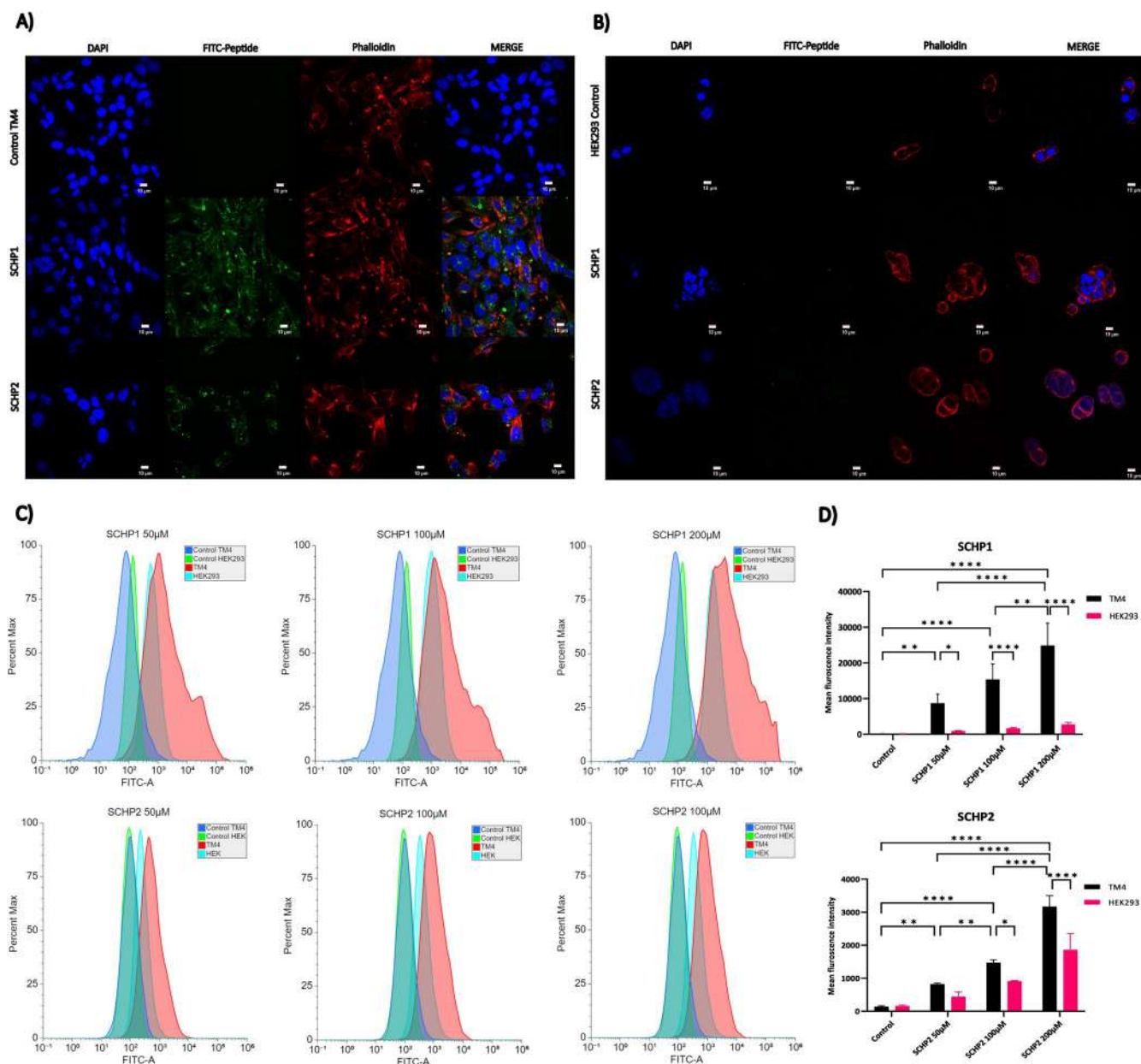
Figure 7. FITC labelled SCHP1 and SCHP2 uptake by TM4 cells (A) and HEK293 cells (B), cells were counter stained with Phalloidin rhodamine for the cytoskeleton and DAPI for the nucleus. C. Histograms of uptake of SCHP1 and SCHP2 by TM4 and HEK293 cells with flow cytometry, D. Quantitation and statistical analysis of the uptake of SCHP1 and SCHP2 by TM4 and HEK293 cells by flow cytometry.
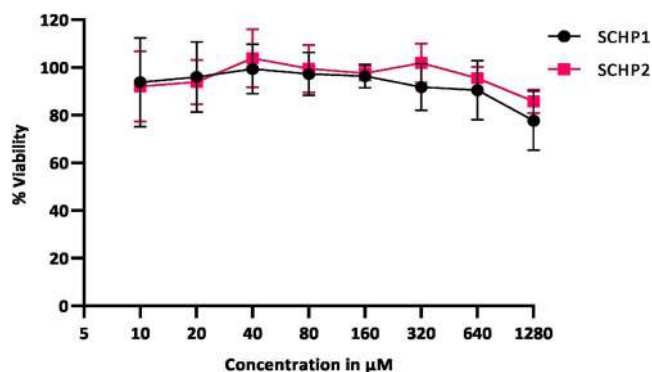

Figure 8. Cytotoxicity of SCHP1 and SCHP2 tested on TM4 cells at two-fold concentrations starting from 10 μM to 1280 μM analysed with MTT assay.

scrambled versions of the SCHP1 and SCHP2 peptides by TM4 cells (Supplementary Figure 4B), as evident from the confocal micrographs. As per the quantitation by flow cytometry, the uptake of SCHP1 and SCHP2 by TM4 cells was significantly higher than control TM4 cells at all three concentrations tested. Further, both the peptide's uptake was increased significantly at 200 μM compared to 50 μM and 100 μM. SCHP1 uptake by HEK293 cells was significantly lower than TM4 cells at all three concentrations, but there was no significant difference compared to control HEK293 cells. SCHP2 uptake by TM4 cells was also significantly higher than HEK293 cells at 100 μM and 200 μM concentrations (Figure 7 C and D). The results indicate that the SCHP1 peptide can efficiently target mouse Sertoli cells (TM4) even at lower concentrations, but higher concentrations of SCHP2 are needed for targeting significantly compared with other cell lines. The exact mechanism of SCHP1 and SCHP2 uptake
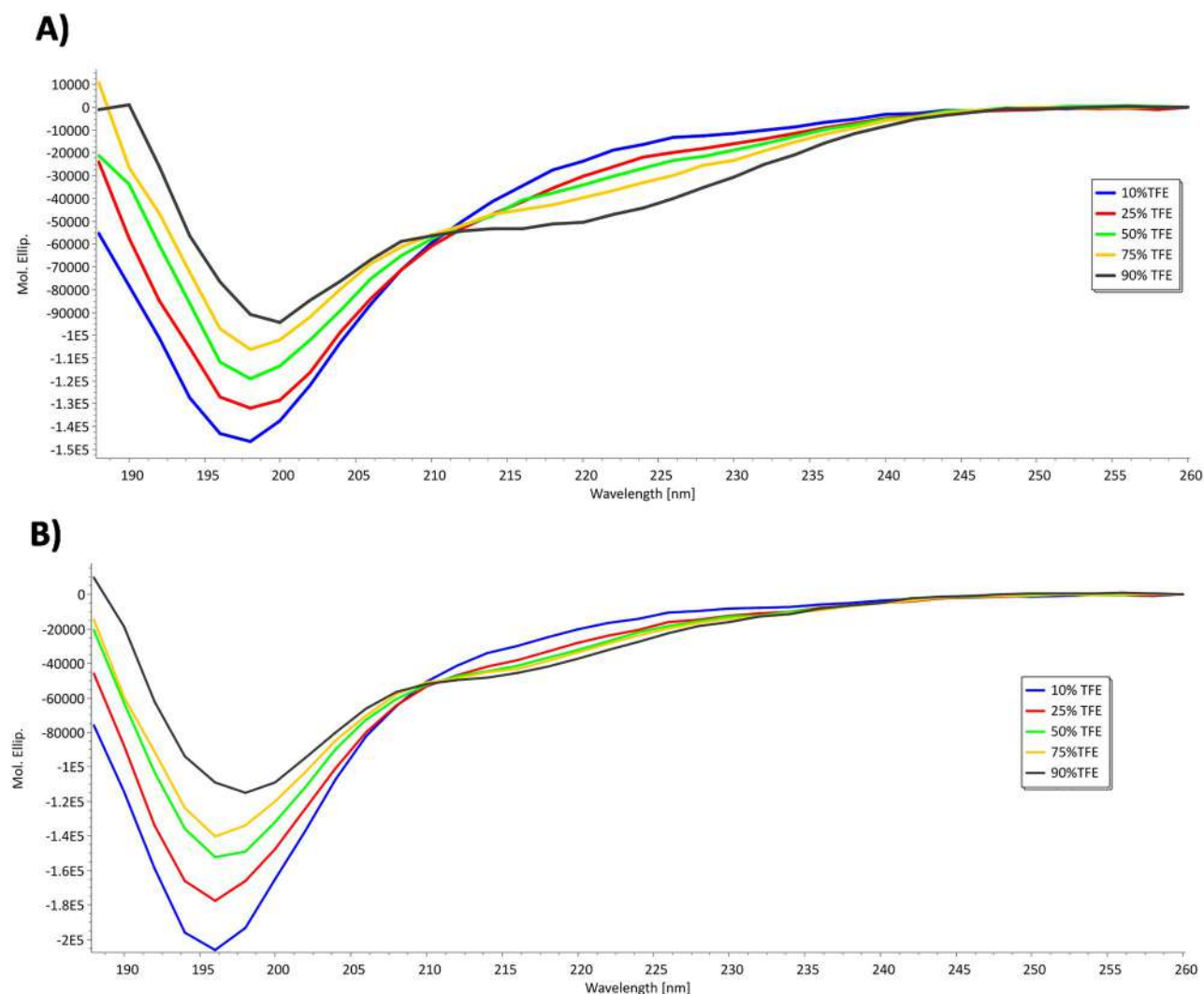
Figure 9. Circular dichroism spectrum of the synthesised SCHP1 (A) and SCHP2 (B). The peptide solution (0.5 mg/mL) was prepared using 10%, 25%, 50%, 75%, and 90% of TFE in water. Spectra were collected every 2 nm from 260 to 190 nm. The CD spectra are recorded as CD (mdeg) and represented as Molar ellipticity.
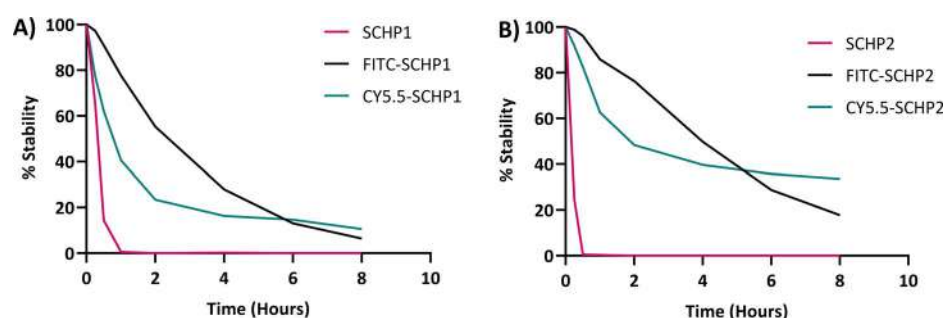

Figure 10. Plasma stability of the unlabelled, FITC labelled and Cy5.5 labelled SCHP1 (A) and SCHP2 (B), at 15 min, 30 min, 1 h, 2 h, 4 h, 6 h and 8 h.

by TM4 cells is not yet studied, but the literature suggests that it could be through a specific kind of molecular signature present on the surface of the cells [41, 42].

Cytotoxicity of the SCHP1 and SCHP2 peptides

Cytotoxicity of SCHP1 and SCHP2 was analysed using MTT cell viability assay at two-fold increasing concentrations. SCHP1 and SCHP2 peptides treated cell was found to be 80% viable at

1280 µM, the highest concentration tested (Figure 8). These results show that the peptides are not cytotoxic and safe for use as cellular-level drug delivery carrier.

Circular dichroism spectroscopy analysis for secondary structure

The secondary structure formation of the SCHP1 and SCHP2 in the environment with different polarities was analysed with Circular Dichroism spectroscopy. Higher percentage of TFE (Trifluroethanol)
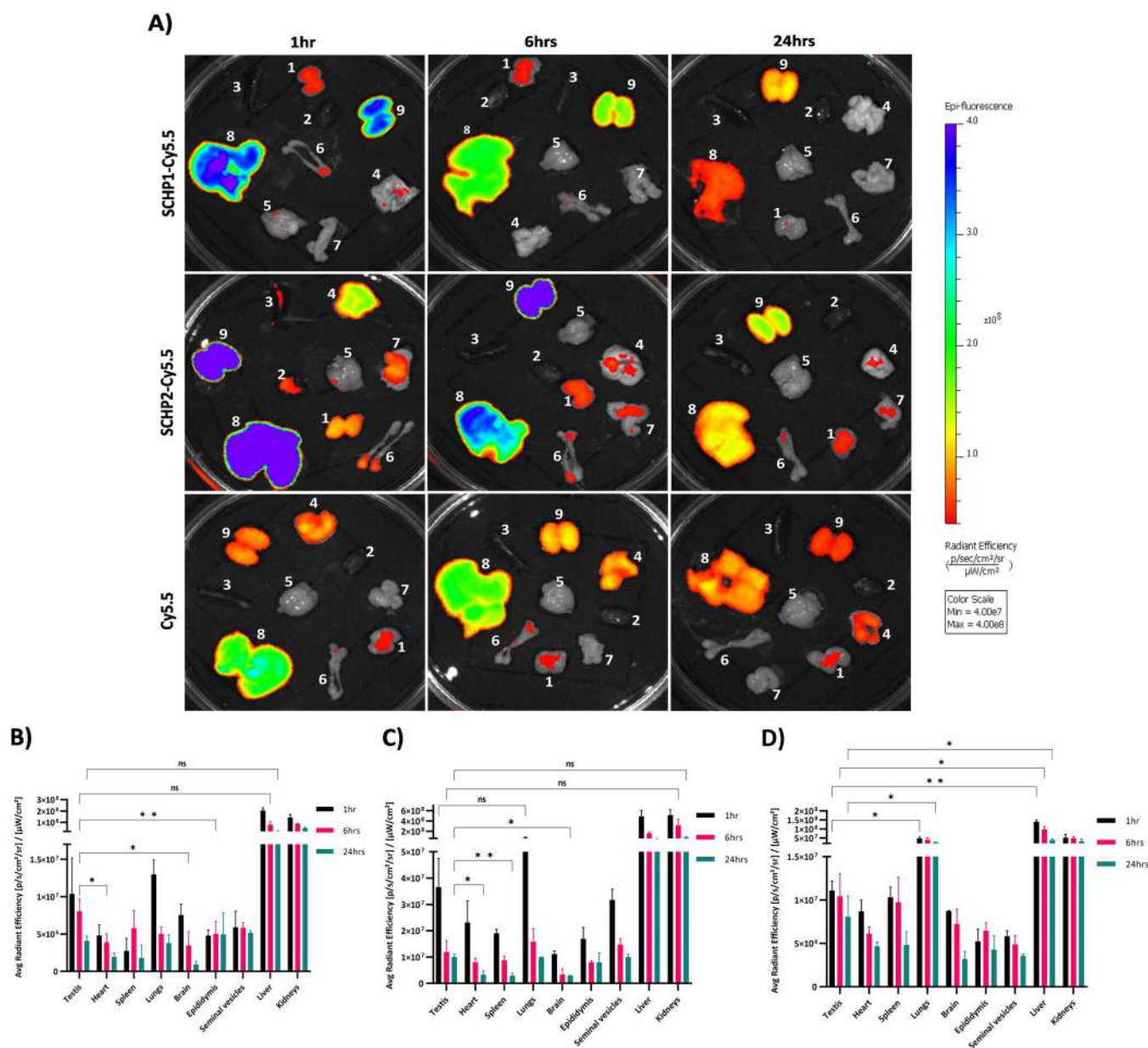
Figure 11. In-vivo bio-distribution of SCHP1-Cy5.5 (A and B), SCHP2-Cy5.5 (A and C), and free Cy5.5 dye (A and D) at 1 h, 6 h, and 24 h time points, 1. Testis, 2. Heart, 3. Spleen, 4. Lungs, 5. Brain, 6. Epididymis, 7. Seminal vesicles, 8. Liver, 9. kidneys. Cy5.5 conjugated peptides were injected intravenously, and after 1 h, 6 h, and 24 h, mice were sacrificed, and organs imaging was performed with Perkin Elmer's IVIS Lumina III in-vivo imaging system and analysed with Living Image software. All data represents the mean ± SD; $n = 3$; * represents $p < 0.05$, ** represents $p < 0.001$, and **** represents $p < 0.0001$ for two-way ANOVA, followed by Dunnett's multiple comparisons test.

mimics membrane bilayer properties by facilitating intramolecular hydrogen bonding [43]. To determine the secondary structure of the SCHP and SCHP2 using CD, the peptides were dissolved in different concentrations of TFE in water. Secondary structures of the SCHP1 (Figure 9A) and SCHP2 (Figure 9B) determined using Reed's reference indicates, at the higher concentration of TFE, there is a decrease in the turns and random structure and an increase in the helix structures (Supplementary Table 3), which indicated that the peptide may form more specific helix structures when present around Sertoli cell membrane which is similar to a higher percentage of TFE.

Plasma stability of the SCHPs

Plasma stability of SCHP1/SCHP2 unlabelled, FITC labelled, and Cy5.5 labelled peptides investigated with RP-HPLC. The unlabelled

SCHPs were not stable even for 30 min in 25% plasma. FITC labelled SCHP1 and SCHP2 were 50% stable up to 2 h and 4 h (Figure 10), respectively. However, Cy5.5 labelled SCHP1 and SCHP2 got rapidly degraded in first 2 h and 50% stable up to 1 h and 2 h, respectively and after 2 h the rate of degradation seems to be decreased. Results show that the FITC and Cy5.5 labelled peptides are more stable compared with unlabelled peptides.

Targeting testis with SCHP1 and SCHP2 peptides in a mouse model

In-vivo bio-distribution and testicular targeting potential of Cy5.5 tagged SCHP1 and SCHP2 peptides were analysed with in-vivo imaging, wherein 20 μg of SCHP1-Cy5.5/SCHP2Cy5.5/Cy5.5 were injected intravenously to the mice and mice were sacrificed after

1 h, 6 h and 24 h to realise the bio-distribution of the peptides. Total Radiant Efficiency [p/s]/[μW/cm²] in the testis is higher compared to other organs except for the kidney and liver in SCHP1 at all the three-time points, SCHP2 uptake is higher in lungs also along with liver and kidney at 1 h which eventually decreases making testis an organ with higher uptake at 6 h and 24 h time point. In contrast, free Cy5.5 dye showed the highest uptake in the kidney, liver, and lungs at all three-time points (Figure 11A). Statistical analysis of the Avg Radiant Efficiency [p/s/cm²/sr]/[μW/cm²] showed that SCHP1 has significantly higher uptake in the testis compared to heart, brain, and epididymis at 6 h time point and higher uptake in the liver is not significant (Figure 11B). Accumulation of SCHP2 in testis is significantly higher compared to the heart, spleen and brain at 24 h time point whereas uptake in lungs and kidney is not significantly higher (Figure 11C). However, in the case of free Cy5.5 dye, there was no significant uptake in the testis at all the time points and uptake by lungs was significantly higher compared to the testis at 1 h and 24 h time points, uptake in the liver was also significantly higher at all the three-time points (Figure 11D). The uptake of the Cy5.5 labelled SCHP1/SCHP2 is found in the organs other than testis may be because of the degradation of the peptide, as the peptide is not stable till 6 h and 24 h. The results of in-vivo bio-distribution suggest that Cy5.5 tagged SCHP1 and SCHP2 have a different pattern of bio-distribution compared to free Cy5.5 dye, distribution of SCHP1, SCHP2 and Cy5.5 is similar in organs involved in the elimination of the drug from the body such as liver, kidney and lungs [44], but compared to other organs uptake of SCHPs is higher in testis which indicated its targeting efficacy towards testis. When SCHP1/SCHP2 were added to the tissue sections of the testis and liver, higher binding of the SCHP1 was observed in testis compared with the liver (Supplementary Figure 5). However, the binding of the SCHP2 was equal to the testis and liver sections (Supplementary Figure 6). The 2X-confocal micrographs of the testis suggest the binding of the peptide on the surface of the Sertoli cells in the seminiferous tubules (Supplementary Figures 5 and 6). The results of the *in vivo* targeting studies suggest SCHP1 as a more promising target over SCHP2. Increasing the stability of the peptides by replacement of L-amino acids which are not required for homing, by D-amino acids, may increase the targeting potential of the SCHPs.

Conclusions

Conventional drug delivery to treat testicular pathologies requires high dosing frequency, resulting in adverse side effects and systemic toxicity. These issues can be circumvented by specifically targeting testicular cells with the help of specific ligands. Cell-homing peptides are potential candidates as a targeted drug delivery agents and are in clinical trials for various cancer targeting. This is the first study demonstrating the identification of Sertoli cells and testis homing peptides using a phage display peptide library. SCHP1 (GSWNTFRAQPTI) and SCHP2 (YSLRLTSVTAPT) were the two highly enriched topmost peptides during in-vitro and in-vivo rounds of biopanning. Ser, Pro, Ala, Thr, Arg, and Lys are the highly enriched amino acid residues in all the common peptides found in the last rounds of in-vitro and in-vivo biopanning. Motif discovery analyses highlighted motifs GSAK, YSLRLT and SVTAPT, are present in the top two selected SCHP1 and SCHP2 concluding that the biopanning procedure is performed with perfect stringency to select the most suitable peptides. Confocal microscopy of the SCHP1 and SCHP2 displaying phage and flow cytometry of FITC labelled synthetic peptides reveals that both the peptides can specifically target TM4 mouse Sertoli cells and not HEK293 cells

and HCASMCs. Synthetic SCHP1 and SCHP2 are non-toxic at the cellular level, and secondary structure prediction suggests the more and helix structure formation in the environment similar to the cell membrane. In-vivo bio-distribution of intravenously injected Cy5.5 labelled SCHPs shows a different pattern than free Cy5.5 dye, and significant enrichment in the testis suggests the testicular targeting potential of the SCHPs. From the results, the selected SCHP1 and SCHP2 peptides have the selective capacity to target Sertoli cells at the in-vitro stage and testis at the in-vivo level. The SCHPs can specifically accumulate in the testis and can serve as an ideal targeting ligand for smart drug delivery to the testis. The efficacy of the male non-hormonal contraceptive drug, like Adjudin, can be increased while decreasing their side effects on other organs. Antioxidants and drugs for treating male infertility whose site of action is inside the testis can also be targeted using these peptides. Plasma stability suggest the stability issues with the selected SCHPs. Various peptides face the same problems of stability, but, addition of a few D-amino acids to the peptide sequence could solve this issue and increase the potential of SCHPs.

Disclosure statement

No potential conflict of interest was reported by the authors.

Author contributions

VD and YJ conceptualised the study and acquired funding from DHR. YJ developed methodologies, performed experiments, and did the formal analysis. VD did project administration and investigation. YJ wrote the original draft, and VD reviewed and edited the final manuscript.

ORCID

Yugandhara Jirwankar (iD) http://orcid.org/0000-0002-6196-1687
Vikas Dighe (iD) http://orcid.org/0000-0001-9718-7358

References

[1] Palermo GD, Kocent J, Monahan D, et al. Treatment of male infertility. Methods Mol Biol. 2014;1154:385–405.

[2]   Gudeloglu A, Brahmbhatt JV, Parekattil SJ. Medical management of male infertility in the absence of a specific etiology. Semin Reprod Med. 2014;32(4):313–318.

[3]   Cocuzza M, Agarwal A. Nonsurgical treatment of male infertility: specific and empiric therapy. Biol Targets Ther. 2007;1(3):259–269.

[4]   Crosnoe LE, Grober E, Ohl D, et al. Exogenous testosterone: a preventable cause of male infertility. Transl Androl Urol. 2013;2(2):106–113.

[5]   Purdue MP, Devesa SS, Sigurdson AJ, et al. International patterns and trends in testis cancer incidence. Int J Cancer. 2005;115(5):822–827.

[6]   Walsh TJ, Grady RW, Porter MP, et al. Incidence of testicular germ cell cancers in U.S. children: SEER program experience 1973 to 2000. Urology United States. 2006;68(2):402–405; discussion 405.

[7]   Hanna NH, Einhorn LH. Testicular cancer – discoveries and updates. N Engl J Med. 2014;371(21):2005–2016.

[8]   Ehrlich Y, Margel D, Lubin MA, et al. Advances in the treatment of testicular cancer. Transl Androl Urol. 2015;4(3):381–390.

[9]   Fung C, Vaughn DJ. Complications associated with chemotherapy in testicular cancer management. Nat Rev Urol. 2011;8(4):213–222.

[10]   Kogan P, Wald M. Male contraception: history and development. Urol Clin North Am. 2014;41(1):145–161.

[11]   Roth MY, Amory JK. Beyond the condom: frontiers in male contraception. Semin Reprod Med. 2016;34(3):183–190.

[12]   Chen H, Mruk DD, Xia W, et al. Effective delivery of male contraceptives behind the blood-testis barrier (BTB) – lesson from adjudin. Curr Med Chem. 2016;23(7):701–713.

[13]   Vasir J, Reddy M, Labhasetwar V. Nanosystems in drug targeting: opportunities and challenges. Curr Nanosci. 2006;1(1):47–64.

[14]   Pasqualini R, Ruoslahti E. Organ targeting in vivo using phage display peptide libraries. Nature. 1996;380(6572):364–366.

[15]   Majumdar S, Siahaan TJ. Peptide-mediated targeted drug delivery. Med Res Rev. 2012;32(3):637–658.

[16]   Smith GP. Filamentous fusion phage: novel expression vectors that display cloned antigens on the virion surface. Science. 1985;228(4705):1315–1317.

[17]   Maruta F, Parker AL, Fisher KD, et al. Use of a phage display library to identify oligopeptides binding to the lumenal surface of polarized endothelium by ex vivo perfusion of human umbilical veins. J Drug Target. 2003;11(1):53–59.

[18]   Lee NK, Kim HS, Kim KH, et al. Identification of a novel peptide ligand targeting visceral adipose tissue via transdermal route by in vivo phage display. J Drug Target. 2011;19(9):805–813.

[19]   Andrieu J, Re F, Russo L, et al. Phage-displayed peptides targeting specific tissues and organs. J Drug Target. 2019;27(5–6):555–565.

[20]   Arap W, Kolonin MG, Trepel M, et al. Steps toward mapping the human vasculature by phage display. Nat Med. 2002;8(2):121–127.

[21]   Kolonin MG, Saha PK, Chan L, et al. Reversal of obesity by targeted ablation of adipose tissue. Nat Med. 2004;10(6):625–632.

[22]   Rajotte D, Ruoslahti E. Membrane dipeptidase is the receptor for a lung-targeting peptide identified by in vivo phage display. J Biol Chem. 1999;274(17):11593–11598.

[23]   Essler M, Ruoslahti E. Molecular specialization of breast vasculature: a breast-homing phage-displayed peptide binds to aminopeptidase P in breast vasculature. Proc Natl Acad Sci U S A. 2002;99(4):2252–2257.

[24]   Zhang L, Hoffman JA, Ruoslahti E. Molecular profiling of heart endothelial cells. Circulation. 2005;112(11):1601–1611.

[25]   Zahid M, Phillips BE, Albers SM, et al. Identification of a cardiac specific protein transduction domain by in vivo biopanning using a M13 phage peptide display library in mice. PLoS One. 2010;5(8):e12252.

[26]   Ghosh D, Peng X, Leal J, et al. Peptides as drug delivery vehicles across biological barriers. J Pharm Investig. 2018;48(1):89–111.

[27]   Fosgerau K, Hoffmann T. Peptide therapeutics: current status and future directions. Drug Discov Today. 2015;20(1):122–128.

[28]   Snow-Lisy DC, Samplaski MK, Labhasetwar V, et al. Drug delivery to the testis: current status and potential pathways for the development of novel therapeutics. Drug Deliv Transl Res. 2011;1(5):351.

[29]   Lee NPY, Mruk DD, Conway AM, et al. Zyxin, axin, and Wiskott-Aldrich syndrome protein are adaptors that link the cadherin/catenin protein complex to the cytoskeleton at adherens junctions in the seminiferous epithelium of the rat testis. J Androl. 2004;25(2):200–215.

[30]   Snow-Lisy DC, Sabanegh ES, Samplaski MK, et al. Anatomical targeting improves delivery of unconjugated nanoparticles to the testicle. J Urol. 2015;194(4):1155–1161.

[31]   McGuire MJ, Li S, Brown KC. Biopanning of phage displayed peptide libraries for the isolation of cell-specific ligands. Methods Mol Biol. 2009;504:291–321.

[32]   Work LM, Nicol CG, Denby L, et al. In vivo biopanning. Methods Mol Med. 2005;108:395–413.

[33]   Peng X, Nguyen A, Ghosh D. Quantification of M13 and T7 bacteriophages by TaqMan and SYBR green qPCR. J Virol Methods. 2018;252:100–107.

[34]   Green MR, Sambrook J. Preparation of single-stranded bacteriophage M13 DNA by precipitation with polyethylene glycol. Cold Spring Harb Protoc. 2017;2017(11):pdb.prot093419.

[35]   Matochko WL, Derda R. Next-generation sequencing of phage-displayed peptide libraries. Methods Mol Biol United States. 2015;1248:249–266.

[36]   He B, Chai G, Duan Y, et al. BDB: biopanning data bank. Nucleic Acids Res. 2016;44(D1):D1127–D1132.

[37]   Schönberger N, Braun R, Matys S, et al. Chromatopanning for the identification of gallium binding peptides. J Chromatogr A. 2019;1600:158–166.

[38]   He B, Chen H, Li N, et al. SAROTUP: a suite of tools for finding potential target-unrelated peptides from phage display data. Int J Biol Sci. 2019;15(7):1452–1459.

[39]   Bailey TL. STREME: accurate and versatile sequence motif discovery. Bioinformatics. 2021;37(18):2834–2840.

[40]   Gupta S, Stamatoyannopoulos JA, Bailey TL, et al. Quantifying similarity between motifs. Genome Biol. 2007;8(2):R24.

[41]   Dougherty PG, Sahni A, Pei D. Understanding cell penetration of cyclic peptides. Chem Rev. 2019;119(17):10241–10287.

[42]   Laakkonen P, Vuorinen K. Homing peptides as targeted delivery vehicles. Integr Biol (Camb). 2010;2(7-8):326–337.

[43]   Haney EF, Vogel HJ. Annual Reports on NMR Spectroscopy. Vol. 65. London (UK): Elsevier, Academic Press; 2009. Chapter 1, NMR of antimicrobial peptides; p. 1–51.

[44]   Garza AZ, Park SB, Kocz R. Drug elimination. Treasure Island (FL): StatPearls Publishing; 2022.

Long-Acting Efavirenz and HIV-1 Fusion Inhibitor Peptide Co-loaded Polymer−Lipid Hybrid Nanoparticles: Statistical Optimization, Cellular Uptake, and *In Vivo* Biodistribution

Dhanashree H. Surve, Yugandhara B. Jirwankar, Vikas D. Dighe,* and Anil B. Jindal*

ACCESS | Metrics & More | Article Recommendations | SI Supporting Information

ABSTRACT: The objective of the present study was to develop long-acting efavirenz (Efa)−enfuvirtide (Enf) Co-loaded polymer−lipid hybrid nanoparticles (PLN) with improved intracellular delivery to target T-cells and macrophage cells located in multiple human immunodeficiency virus sanctuaries. The Box−Behnken design was utilized to optimize three high-risk factors, namely, Efa amount, sonication time for primary emulsion, and sonication time for aqueous nanodispersion obtained from preliminary studies. Lyophilized Efa−Enf Co-loaded PLN using trehalose elicited spherical morphology, drug amorphization on incorporation, and absence of drug-excipient interaction. *In vitro* release studies revealed an sustained release of both the drugs from PLN with the differential release profile. Efa−Enf Co-loaded PLN exhibited low hemolytic, platelet and leukocyte aggregation as well as low cytotoxicity in Jurkat E6.1 T-cells and U937 macrophage cells. Circular dichroism spectra confirmed the presence of an α-helix form of Enf after encapsulation in PLN. Coumarin-6-loaded PLN exhibited enhanced cellular uptake in Jurkat E6.1 T-cells and U937 macrophage cells in comparison to free coumarin-6, as evidenced by fluorescence microscopy and flow cytometry. *In vivo* biodistribution studies after intravenous administration of near-infrared dye-loaded PLN (surrogate for Efa−Enf PLN) revealed non-uniform distribution within 2 h in the order of spleen ≥ liver > lymph node > thymus > lungs > female reproductive tract (FRT) > heart > kidneys > brain. However, subcutaneous administration caused non-uniform biodistribution after 3 days, eliciting a long-acting slow release from the injection site depot until day 5 in the infection-spread site (lymph nodes and FRT), reservoir sites (liver and spleen) and the difficult-to-access site (brain). Furthermore, it presents a vital illustration of the available tissue-specific drug concentration prediction from simulated surrogate PLN.

KEYWORDS: *fusion inhibitor peptide, polymer−lipid hybrid nanoparticle (PLN), long-acting, simulation, Jurkat E6.1 cells, U937 macrophage*

1. INTRODUCTION

Oral combination antiretroviral therapy (cART, also known as highly active ART or HAART) was invented in 1995[1] because of consistent attempts for the treatment of the life-threatening human immunodeficiency virus (HIV) infection. It consists of two or more drugs from the divergent antiretroviral (ARV) class targeting different stages of the HIV life cycle, which enabled increased life expectancy of HIV patients.[2] However, oral cART is associated with drawbacks including frequent dosing,[3] inaccessibility, abysmal adherence,[4,5] and pruned bioavailability of cART,[6] thereby ensuing an inadequate therapeutic concentration of cART at inaccessible sites, viral rebound, and drug resistance.[7] Parenteral administration of ARV nanoformulations *via* the subcutaneous (SC) or intramuscular (IM) route may lead to a long-term slow effective release for weeks or months by improving the pharmacokinetics, biodistribution, and therapeutic efficacy against the HIV infection.[8,9] Moreover, long-acting ARV (LA ARV) nano-

formulations form a primary depot (injection site) and a secondary depot (infiltered immune cells at the administration site or tissue lymphocytes)[10,11] and deliver ARV drugs to the major difficult-to-access sites (brain and thymus), HIV infection sites (rectum or vagina), spread sites (lymphatic vessel and lymph node), and reservoir sites (liver and spleen) through the lymphatic-circulatory loop.[9] After the successful ATLAS and FLAIR phase III clinical trials, Cabenuva containing two long-acting (LA) nanocrystal suspensions, namely, cabotegravir and rilpivirine, has been recently

approved by Health Canada for once-monthly administration by the IM route.[12] Cabotegravir- or rilpivirine-loaded LA nanosuspensions showed a plasma half-life of 25−40 and 40 days, respectively, after IM administration to healthy individuals.[13] Profuse preclinical success for LA polymer[14−16] or lipid nanocarriers[17−19] incorporating a single ARV nanoformulation or a combination of ARV nanoformulations has been established for maraviroc, tenofovir, emtricitabine, bictegravir, lopinavir, elvitegravir, atazanavir, and ritonavir.[9]

Furthermore, drugs with poor oral bioavailability, aqueous solubility, rapid first-pass metabolism, and a longer half-life are eligible for presentation through LA nanoformulations.[9] Efavirenz (Efa) is a non-nucleoside reverse transcriptase inhibitor (NNRTI) and considered under first-line HAART.[20] It exhibits a poor aqueous solubility (8.55 μg/mL) and a log P of 4.6[21] and is rapidly metabolized by first-pass metabolism.[22] However, Enfuvirtide (Enf) is a fusion inhibitor peptide approved by USFDA in 2003.[23] It is a 36 amino acid peptide with a molecular weight of 4.5 kDa, which blocks the fusion of viral and cell membranes by binding to glycoprotein-41 with poor oral bioavailability[24] and rapid catabolism by peptidases and proteinases prominently in hepatic and kidney cells.[25,26] Moreover, codelivery of the NNRTI and HIV-1 fusion inhibitor could massively improve the anti-HIV effect of individual drugs.[27]

Therefore, the objective of the present study emphasizes on effective intracellular delivery of the developed LA Efa−Enf Co-loaded polymer−lipid hybrid nanoparticles (PLN) to immune cells (macrophages and T-cells) predominantly responsible for secondary depot genesis. Additionally, it intends to elucidate the biodistribution of LA Efa−Enf Co-loaded PLN in BALB/c mice.

2. MATERIALS AND METHODS

2.1. Materials. Efa was a kind gift sample from Ranbaxy Laboratories Ltd. (Gurgaon, India). Enf was purchased from ProSpec Protein Specialists (Rehovot, Israel). Stearic acid, docusate sodium, dichloromethane, sodium dihydrogen orthophosphate, and mannitol were purchased from S D Fine-Chem Limited (Mumbai, India). Soy lecithin, dialysis bag [a molecular weight cutoff (MWCO) of 12−14 kDa], Dulbecco's phosphate-buffered saline (DPBS), and glutaraldehyde (25% w/w) were purchased from HiMedia Laboratories Pvt. Ltd. (Mumbai, India). Tween 80, trehalose, and thiazolyl blue tetrazolium bromide (MTT) were obtained from Sisco Research Laboratories Pvt. Ltd. (Mumbai, India). Cremophor HS-15 was a kind gift sample from BASF Chemicals Company (Navi Mumbai, India). Branched polyethyleneimine (a molecular weight of 25,000), poly(lactic-co-glycolic) acid (PLGA) (50:50), coumarin-6, and a cell proliferation WST-1 kit were procured from Sigma-Aldrich Chemicals Company (Missouri, United States). Ficoll-Paque PLUS was procured from GE Healthcare (Chicago, United States). Ethanol was purchased from Jabsen and Jabsen Co. (GmbH, Germany). RPMI 1640 and foetal bovine serum (FBS) were procured from Gibco Biosciences (New York, United states). Phorbol-12-myristate-13-acetate (PMA) was procured from Cayman Chemical Company. U937 and Jurkat E6.1 suspended cell lines and BALB/c mice were kind gifts from the ICMR-National Institute for Research in Reproductive Health (Mumbai, India). Lactose and sucrose were procured from Central Drug House (New Delhi, India). XenoLight 1,1′-dioctadecyl-3,3,3′,3′-tetramethylindotricarbocyanine iodide [DiR,

(DilC18(7)] was procured from PerkinElmer (Waltham, United States), and ultrapurified water was obtained from Milli-Q systems (Millipore GmbH, Germany).

2.2. Preparation of Efa−Enf Co-loaded PLN. Efa−Enf Co-loaded PLN were prepared by the double-emulsion solvent evaporation method as described previously with some modifications.[28] Briefly, Efa (50−100 mg) and stearic acid (45 mg) equivalent to a molar ratio of 1:1, soy lecithin (200 mg), and PLGA (10 mg) were dissolved in dichloromethane (5 mL) to obtain an organic phase. Enf (2 mg) was dissolved in 1 mL of phosphate buffer (10 mM, pH 6.5) and added dropwise to the abovementioned organic phase and probe-sonicated using a probe sonicator (Sonics & Materials, Inc., USA) at 4 °C for 90 s (500 W, 25% amplitude) to obtain the water-in-oil (w/o) primary emulsion. The primary emulsion was then added dropwise to 30 mL of the external aqueous phase containing 2% w/v cremophor HS-15 using a homogenizer (IKA T 10 basic ULTRA-TURRAX) for 600 s at 15,000 rpm to obtain the water-in-oil-in-water (w/o/w) double emulsion. The organic phase of the w/o/w double emulsion was evaporated using a Buchi Rotavapor rotary evaporator at 30 °C for 20 min to obtain an aqueous nanodispersion. The aqueous nanodispersion was then probe-sonicated for 360 s at 4 °C (500 W, 25% amplitude) and was stored at 4 °C until further evaluation.

Coumarin-6 and DiR-loaded PLN were prepared by a similar procedure as mentioned above by dissolving coumarin-6 (1 mg) or DiR (0.5 mg) in the organic phase after omitting Efa and Enf to yield dye-loaded PLN. Coumarin-6 and DiR-loaded PLN served as surrogates of Efa−Enf PLN to depict cellular uptake and *in vivo* biodistribution studies, respectively.

2.3. Optimization of Efa−Enf Co-loaded PLN Using the Box−Behnken Design. Optimization and statistical analysis of Efa−Enf Co-loaded PLN were done by the Box−Behnken design using Design-Expert software version 8.0.7.1 (Stat-Ease Inc., Minneapolis, MN). Based upon initial screening, the three most significant factors, namely, Efa amount (A), sonication time for the oil-in-water (o/w) primary emulsion (B), and sonication time for the w/o/w aqueous nanodispersion (C) in the formation of Efa−Enf Co-loaded PLN, were identified. However, the amount of Enf (2 mg), stearic acid (45 mg), PLGA (10 mg), soy lecithin (200 mg), Cremophor HS-15 (600 mg), dichloromethane (5 mL), and the external aqueous phase (30 mL) and the homogenization speed and time (15,000 rpm, 10 min, respectively) were kept constant. A valid design space was generated using 3 center points for replication and 12 mid points of each edge of a cube. Three independent factors were varied at three levels as shown in Table 1 to generate 15 experimental runs (Table S1). The main effect, interaction

Table 1. Independent and Dependent Factors in the Box−Behnken Optimization Design

Box−Behnken Design			
		levels	
independent factors	−1	0	+1
A = Efa amount (mg)	50	75	100
B = sonic time for the w/o primary emulsion (s)	0.30	1.30	3.00
C = sonic time for the w/o/w emulsion (min)	1.30	3.00	6.00
dependent factors			
Y_1 = Efa % EE $\quad$ Y_2 = Enf % EE $\quad$ Y_3 = particle size $\quad$ Y_4 = PDI			

effect, and the quadratic effect of independent factors were observed on dependent factors such as Efa % entrapment efficiency (EE) (Y_1), Enf % EE (Y_2), particle size (Y_3), and polydispersity index (PDI) (Y_4) for Efa−Enf Co-loaded PLN, and suitable response surface graphs, polynomial equations, and mathematical models were generated. After generating the model based on the relation of independent and dependent factors, each dependent factor or response was optimized based on the desirability function. Validation of the model was performed by matching the predicted and obtained values of dependent factors for specific independent factors of PLN eliciting the highest desirability function.

2.4. Characterization of Efa−Enf Co-loaded PLN. *2.4.1. Particle Size, PDI, and Zeta Potential.* The aqueous nanodispersion of Efa−Enf Co-loaded PLN, coumarin-6-loaded PLN and DiR-loaded PLN obtained in Section 2.2 was centrifuged at 17,000 rpm at 4 °C for 25 min using an Eppendorf 5430 R centrifuge, followed by separation of the supernatant from pellets. The pellet was redispersed and diluted using Milli-Q water. The particle size, PDI, and zeta potential of diluted samples were measured by photon correlation spectroscopy using a Malvern Nano ZS (Malvern Instruments Ltd., UK) at 30 °C.

2.4.2. Percentage Entrapment Efficiency. The supernatant obtained after centrifugation as described above was suitably diluted and analyzed using high-performance liquid chromatography (HPLC) as reported previously by our group[29] and a spectrophotofluorimeter to determine the amount of Efa and Enf, respectively. The percentage EE was calculated using i.

$$\% \text{ EE} = \frac{\text{total amount of drug added} - \text{amount of drug in the supernatant}}{\text{total amount of drug added}} \times 100$$

(i)

2.4.3. Field Emission Scanning Electron Microscopy. Lyophilized Efa−Enf Co-loaded PLN (2 mg) were placed onto the carbon tape attached to a metal stub and gold-coated for 45 s using a Quorum Technologies Q150TES sputter coater (East Sussex, England). Gold-coated nanoparticles were then analyzed using an FEI scanning electron microscope (Hillsboro, Washington) at 20 kV high vacuum, 60,000× magnification with a spot size of 8.0, and a scale of 1−3 μm.

2.4.4. Differential Scanning Calorimetry. Differential scanning calorimetry (DSC) was performed using a DSC-60 Plus by Shimadzu (Kyoto, Japan). The DSC thermogram of Efa, Enf, stearic acid, PLGA, soy lecithin, cremophor HS-15, trehalose, and lyophilized Efa−Enf Co-loaded PLN was obtained by adding 5 mg of each sample in an aluminum pan and heating the individual sample pan at a rate of 10 °C/min between 30 °C−300 °C with an empty aluminum pan as a reference under nitrogen purge (20 mL/min).

2.4.5. Fourier Transform Infrared Spectra. Fourier transform infrared (FTIR) spectra of 10 mg each of Efa, Enf, stearic acid, PLGA, soy lecithin, cremophor HS-15, trehalose, and their physical mixture and lyophilized Efa−Enf Co-loaded PLN were recorded using a Bruker alpha-one FTIR spectrophotometer (Bruker Optik, Germany) after placing the individual sample (5 mg) on a ZnSe sample crystal and scanning the spectra from 3800 to 600 cm^{-1}.

2.5. Circular Dichroism Analysis. The secondary structure of free Enf and Enf loaded in PLN was analyzed using a Jasco circular dichroism (CD) instrument (Easton, United States). CD analysis of both the samples was done in phosphate buffer (10 mM, pH 6.8) at 25 °C with a scanning speed of 50 nm/min and a cell length of 0.1 cm.

2.6. Lyophilization Studies. *2.6.1. Freeze−Thaw Studies.* Freeze−thaw studies were carried out as a pretest to screen various cryoprotectants, namely, lactose, sucrose, mannitol, and trehalose for lyophilization of Efa−Enf Co-loaded PLN. The aqueous nanodispersion of Efa−Enf Co-loaded PLN was frozen for 24 h at −80 °C in a deep freezer (Thermo Fisher Scientific, USA) after dissolving the individual cryoprotectant (3.2% w/v) in a glass vial. Frozen samples were kept at room temperature for thawing. The particle size and PDI of the Efa−Enf Co-loaded nanodispersion were determined as described in Section 2.4.1.

2.6.2. Lyophilization Studies. The aqueous nanodispersion of Efa−Enf Co-loaded PLN (25 mL) was centrifuged at 48,000 rpm for 20 min to separate the PLN. Then, PLN were redispersed in 7.5 mL of Milli-Q water and frozen at −80 °C in a deep freezer (Thermo Fisher Scientific, USA) for 12 h after dissolving 20% w/v trehalose. Lyophilization was carried out in a Labconco freeze drier (FreeZone 2.5, USA) for 48 h at −54 °C and −0.018 mbar. The lyophilized nanoparticles were reconstituted (30 mg/mL) with Milli-Q water. The particle size, PDI, and zeta potential were determined as mentioned in Section 2.4.1. An aliquot of reconstituted nanoparticles was extracted with acetonitrile (800 μL) and bath-sonicated for 5 min. Then, the extract was centrifuged at 15,000 rpm for 10 min, suitably diluted, and analyzed by HPLC and spectrofluorimetry to determine the Efa and Enf contents, respectively.

2.7. *In Vitro* Drug Release Studies. *In vitro* release of Efa−Enf Co-loaded PLN was carried out using the dialysis bag method as described previously.[21] Briefly, the Efa−Enf Co-loaded PLN dispersion equivalent to 2.1 mg and 34 μg of Efa and Enf, respectively, was filled in a dialysis bag (an MWCO of 12−14 kDa, HiMedia Laboratories. Pvt. Ltd., Mumbai, India). The dialysis bag was closed from both sides and suspended in 30 mL of phosphate buffer (10 mM, pH 7.4) in a shaking water bath (100 rpm, 37 °C). The sample (3 mL) was withdrawn at predetermined time points (0.5, 2, 4, 8, 12, 24, and 33 h) and replaced with an equivalent amount of a fresh dissolution medium. The samples were then diluted appropriately and analyzed using HPLC and a spectrofluorophotometer to determine the release of Efa and Enf, respectively, from the PLN. The study was carried out in triplicate.

2.8. Blood Compatibility Studies. *2.8.1. In Vitro Hemolysis Studies.* *In vitro* hemolysis studies were carried out as reported previously with some modifications.[30] Blood was collected from Wistar rats in tubes containing ethylenediaminetetraacetic acid solution (10% w/v, a blood-to-anticoagulant ratio of 50:1) and centrifuged at 1000 rpm for 5 min. After centrifugation, the red blood cells (RBCs) were collected and rinsed with normal saline and further centrifuged to obtain RBC pellet. The RBC pellet was then diluted with 200 μL of normal saline. Efa−Enf PLN were suitably diluted with normal saline to obtain a final concentration of Efa and Enf between 20 and 60 and between 0.1 and 0.3 μg/mL, respectively. Similar dilutions were made for blank PLN to serve as the control. To 100 μL of each dilution, 100 μL of the above mentioned RBC suspension was added and incubated at 37 °C for 30 min. Normal saline and distilled water were used as the negative control and positive control, respectively. After 30 min, normal saline was added up to 1 mL. Each sample was centrifuged at 1000 rpm for 5 min, and 200 μL of the

supernatant was analyzed using an Epoch ELISA plate reader (BioTek, Winooski, United States) at 540 nm. The percentage hemolysis was calculated using ii.

$$\text{Hemolysis (\%)} = \frac{\text{OD sample} - \text{OD negative control}}{\text{OD positive control} - \text{OD negative control}} \times 100$$

(ii)

2.8.2. RBC, White Blood Cell, and Platelet Aggregation Studies. Treated RBC pellets were suitably diluted (20 times in normal saline), and 100 μL of the RBC suspension was fixed in 100 μL of glutaraldehyde solution (2.5% in normal saline). The RBC−glutaraldehyde solution (50 μL) was added onto a glass coverslip and allowed to dry overnight at 4 °C. The samples were washed thrice with normal saline, dehydrated with 50 and 100% ethanol sequentially, and coverslips were allowed to dry at 37 °C. The samples were placed onto the carbon tape attached to a metal stub and gold-coated for 45 s using a Quorum Technologies Q150TES sputter coater (East Sussex, England). Gold-coated treated RBCs were then analyzed using the FEI scanning electron microscope (Hillsboro, Washington).

Further, platelet and white blood cell (WBC) aggregation studies were carried out to evaluate the blood compatibility of PLN. The platelets and WBCs were separated by layering rat blood suitably diluted with normal saline (1:1 ratio) on 3 mL of Ficoll-Paque Plus and centrifuging at 400g for 30 min. For aggregation studies, 50 μL of WBCs or platelet suspension was treated with 50 μL of Efa−Enf Co-loaded PLN equivalent to 40 μg of Efa and 0.78 μg of Enf at 37 °C for 1 h. Polyethylenimine (PEI) and normal saline were used as the positive control and negative control, respectively. The treated cells were then prepared for scanning electron microscopy (SEM) analysis similar to RBCs as stated above.[30]

2.9. Cytotoxicity and Cellular Uptake of Efa−Enf Co-loaded PLN. *2.9.1. Cells.* Jurkat E6.1 T and U937 suspended cell lines were cultured in RPMI 1640 media enriched with FBS (10% w/v) in a T-75 culture flask at 37 °C and 5% v/v CO_2 for 6 days until an optimal cell density of 11×10^6 cells/mL was obtained.

2.9.2. Cytotoxicity Studies. 2.9.2.1. Cytotoxicity Studies in Jurkat E6.1 T-Cells. Jurkat E6.1 T-cells (10^4 cells/well) were suitably seeded in a 96-well plate. The cells were incubated with 50 μL of blank PLN, Efa PLN, Enf PLN, and Efa−Enf PLN equivalent to Efa (7.92, 15.84, 31.68, 63.36, 126.71, and 253.43 μM) and Enf (0.898, 0.449, 0.225, 0.112, 0.056, and 0.028 μM) for 24 h. Then, 10 μL of the cell proliferation WST-1 reagent was added in each well and incubated for 4 h. The 96-well plate was kept on a plate shaker for 10 min. Then, the absorbance was recorded at 440 nm using an Epoch ELISA plate reader (BioTek, Winooski, United States).

2.9.2.2. Cytotoxicity Studies in U937 Cells. U937 macrophage cells (10^5 cells/well) suspended in complete RPMI 1640 media containing PMA (0.1 ng/mL) were seeded in a 96-well plate and incubated in a CO_2 incubator (5% v/v CO_2, 37 °C) overnight. The media were removed and treated with 100 μL of blank PLN, Efa PLN, Enf PLN, and Efa−Enf PLN dispersed in RPMI 1640 media equivalent to Efa (6.18, 12.37, 24.74, 49.49, 98.99, and 197.92 μM) and Enf (0.045, 0.089, 0.179, 0.357, 0.714, 1.42, 2.86, and 5.72 μM) for 24 h. Then, the

supernatant was removed, and the cells were treated with 100 μL of the MTT reagent (500 μg/mL) for 4 h; the reagent was removed, and 100 μL of dimethyl sulfoxide was added to dissolve the formed formazan crystals. Then, the absorbance was recorded at 570 nm using the Epoch ELISA plate reader (BioTek, Winooski, United States).

2.9.3. Fluorescence Microscopy. Jurkat E6.1 T-cells and U937 macrophage cells (10^6 cell count) were seeded in 1.5 mL microcentrifuge tubes. Then, the cells were incubated with 100 μL of coumarin-6 PLN suitably diluted with the RPMI 1640 medium without FBS to obtain a coumarin-6 concentration of 100 ng/mL at 37 °C for 1 or 4 h in 5% (v/v) CO_2. Then, the microcentrifuge tubes were centrifuged at 3000 rpm for 5 min to obtain cell pellets. The pellet was then washed with DPBS twice and counterstained with 4′,6-diamidino-2-phenylindole (DAPI, 300 ng/mL) by incubating for 15 min in the dark. The cells were again washed and resuspended using DPBS, whose aliquot was mounted onto a glass slide and fixed using 4% paraformaldehyde. The cells were then observed under a Carl ZEISS Axio fluorescence microscope (Jena, Germany), and the images were processed using AxioVision Rel.4.5 software.

2.9.4. Flow Cytometry. Coumarin-6 PLN cellular uptake quantification was performed using a flow cytometer. Cells (10^7) were incubated with 100 μL of free coumarin-6 or coumarin-6 PLN in DPBS at 37 °C for 1 and 4 h and analyzed using an FACSAria SORP with an argon laser (Becton, Dickinson, San Jose, CA, USA). A total of 10,000 events were recorded in the flow cytometer and the cell sorter (FACS). The data was analyzed using Diva 6.1.3 software (BS, San Jose, CA, USA).

2.10. *In Vivo* Biodistribution. All animal procedures were approved by the Institutional Animal Ethics Committee of the National Centre for Preclinical Reproductive and Genetic Toxicology, ICMR, National Institute for Research in Reproductive Health, Parel, Mumbai (protocol no. IAEC no 14-19). Female BALB/c mice 8−12 weeks old were utilized for the study. The animals were divided into four groups. DiR PLN were administered to group I intravenously *via* the tail vein and subcutaneously *via* the right flank to groups II, III, and IV. Whole-body imaging was carried out using a PerkinElmer IVIS Lumina S5 (Waltham, United States) at predetermined time points for group I (0, 1, 2, 4, 8, 10, and 24 h), group II (0, 1, 2, 4, 8, 10, 24, and 48 h), group III (0, 1, 2, 4, 8, 10, and 72 h), and group IV (0, 1, 2, 4, 8, 10, 24, 48, 72, 96, and 120 h). The animals were sacrificed after 24 h of group I and II, 72 h of group III, and 120 h of group IV. The fluorescence intensity of different organs including the brain, heart, kidneys, liver, lung, axillary lymph nodes, spleen, thymus, and female reproductive tract (FRT) was measured using the PerkinElmer IVIS Lumina S5 (Waltham, United States).

2.11. Prediction of the Dose and Target Site Drug Level by Simulation of the DiR PLN Biodistribution Profile. The *in vivo* biodistribution of DiR PLN was used as a surrogate to Efa-Enf PLN, wherein a fraction of DiR PLN reaching various tissues were utilized to predict the dose of Efa and Enf PLN required to achieve the minimum effective concentration (MEC) of the individual drug using iii.

$$\text{Predicted dose (}\mu g\text{)} = \frac{\text{MEC (}\mu g/mL\text{)}}{\text{mean of available fraction of DiR PLN per gram organ weight}} \times \text{blood volume per gram target tissue weight (mL/g)}$$
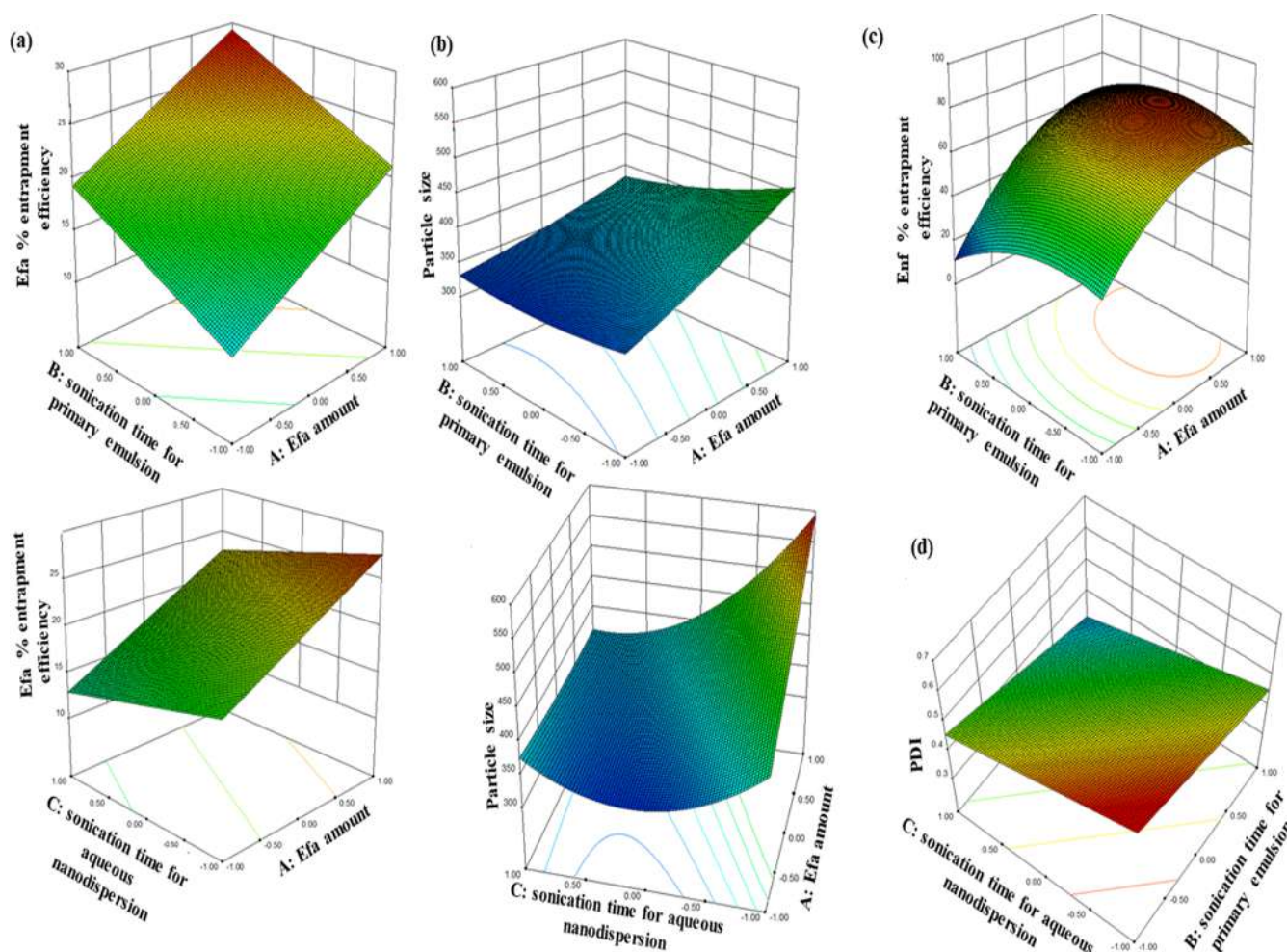
(iii)

Figure 1. Box–Behnken 3D response surface plot. (a) Percentage EE Efa, (b) particle size, (c) percentage EE Enf, and (d) PDI.

2.12. Statistical Analysis.

Statistical data analysis was performed using a student t-test with $p < 0.05$ as a minimal level of significance. The results were expressed as the mean ± standard deviation (SD) obtained from three separate experiments ($n = 3$). Mathematical fit functions were performed by ANOVA analysis.

3. RESULTS AND DISCUSSION

3.1. Optimization of Efa–Enf Co-loaded PLN using the Box–Behnken Design.

The Box–Behnken design is a 3^{k-p} fractional factorial design that comprises the higher number of runs with a high degree of freedom and precise optimization. Further, the design is spherical and rotatable, which aids in orthogonal blocking. The main effect, interaction effect, and the quadratic effect independent variable, that is, Efa amount (A), sonication time for the w/o primary emulsion (B), and sonication time for the aqueous nanodispersion (C), were examined on percentage EE of Efa (Y_1), percentage EE of Enf (Y_2), particle size (Y_3), and PDI (Y_4) (Table S1). The quadratic model was significant for Y_2 (R^2—0.9817) and Y_3 (R^2—0.932), while a linear model with an insignificant lack of fit was established for Y_1 (R^2—0.6225) and Y_4 (R^2—0.7596) to navigate the design space. Further, every factor was found to have a significant impact ($p < 0.05$) on each dependent factor as determined by ANOVA (Table S2). The first-order polynomial equations obtained for the responses Y_1 and Y_4 were as follows

$$Y_1 = 20.274 + 4.9878A + 4.069 \times B - 2.379 \times C \quad \text{(iv)}$$

$$Y_4 = 0.4571 + 0.026 \times A - 0.072 \times B - 0.07 \times C \quad \text{(v)}$$

The negative effect (negative coefficient in the linear equation) on Y_1 and Y_4 was observed with increasing sonication time of double emulsion because of an increase in the total energy of the system, leading to increased drug expulsion and a decrease in PDI of the PLN, which is in agreement with previous reports.[31,32] However, second-order polynomial vi and vii for Y_2 and Y_3, respectively, signify that the single-coefficient terms depict the main effect and the combination term indicates the interaction effect. The coefficient of C is the lowest and hence exerted an insignificant effect on response Y_2. However, the coefficient of the combination terms $A \times B$ and $A \times C$ is the highest and thus has a profound effect on Y_2 and Y_3, respectively.

$$
\begin{aligned}
Y_2 = {} & 64.18 + 21.16 \times A - 5.561 \times B - 0.097 \times C \\
& + 5.1483 \times A \times B + 3.3375 \times A \times C \\
& + 2.1443 \times B \times C - 15.21A^2 - 10.1B^2 \\
& + 2.5068 \times C^2 \quad \text{(vi)}
\end{aligned}
$$

$$Y_3 = 360.375 + 42.518 \times A - 21.42 \times B - 65.27 \times C$$
$$- 16.47 \times A \times B + 49.06 \times A \times C$$
$$+ 13.5 \times B \times C + 4.9399 \times A^2 + 9.7984 \times B^2$$
$$+ 66.602 \times C^2 \qquad\qquad (vii)$$

The main effect of an independent factor on an individual response was analyzed by perturbation plots (Figure S1), while three-dimensional (3D) model graphs were used to determine the interaction effect of two independent variables on dependent factors at a fixed level of the third independent variable (Figure 1). It was observed that at a fixed level of sonication time for the aqueous nanodispersion, Y_1 and Y_4 increased with an increase in both Efa amount and sonication time for the w/o primary emulsion. Increased sonication of the primary emulsion caused optimum emulsification of amorphonized Efa with lipids in the primary emulsion causing efficient particle interaction and enhanced solubilization of Efa in soy lecithin, making drug leakage evitable.[33,34] On the contrary, the aftermath of increased energy of the w/o primary emulsion was enhanced instability (increased Y_4).[35] An increase in sonication time of the w/o primary emulsion at a fixed level of sonication time for the aqueous nanodispersion led to a decrease in the encapsulation of Enf, while an increase in Efa amount led to an increase in encapsulation of Enf because of reduced diffusion of the drug through the hydrophobic core. On the other hand, the sonication time of the aqueous nanodispersion depicted an inverse relation with Y_2, Y_3, and Y_4. However, a higher collisional frequency of PLN accompanied with an increase in total energy of the w/o/w aqueous nanodispersion, increased particle size, and PDI after a specific level.[35] However, the particle size of PLN increased with an increase in Efa because of enhanced encapsulation of Efa.[36]

The optimal solution was obtained by setting the target of Efa amount and sonication time for the w/o primary emulsion in range, and the target for sonication time for the aqueous nanodispersion was set at 0 level to achieve stable PLN with the goal of minimum error propagation of Enf and particle size, a minimum standard error, a maximum percentage EE of Efa and Enf, and a minimum particle size and PDI. The solution obtained with a desirability next to 1 ($D = 0.883$) with the optimized level for each factor being 0.83, 1, and 0.20 for Efa amount, sonication time for the primary emulsion, and sonication time for the aqueous nanodispersion, respectively, was adopted and screened to calculate the percentage bias between the predicted and actual values (Table 2).

The optimized solution was utilized to prepare surrogate PLN as described in Section 2.2 for cellular uptake and *in vivo* biodistribution studies (Table S3).

3.2. Characterization of Efa−Enf Co-loaded PLN. Field emission scanning electron microscopy analysis of the prepared

Table 2. Validation of the Box−Behnken Design

parameter	predicted	actual	mean % bias
Efa % EE	28.0	27.1 ± 0.78[a]	3.12
Enf % EE	64.9	69.7 ± 3.79[a]	7.2
particle size	362.2	346.4 ± 30.41[a]	4.4
PDI	0.39	0.440 ± 0.06[a]	11.9

[a]Each value represents the mean ± SD, $n = 3$, $p < 0.001$ for the one-tailed paired t-test.

Efa−Enf Co-loaded PLN revealed the spherical shape of nanoparticles (Figure 2a). While, DSC thermograms of different components of PLN and Efa−Enf Co-loaded PLN are shown in Figure S2a. It revealed sharp endothermic peaks of stearic acid, PLGA, Efa, and cremophor HS-15 at 59.3, 41.4, 139.3, and 30.5 °C, respectively, corresponding to their melting point.[37−39] Enf and soy lecithin exhibited a broad peak at 25.8 and 158.1 °C, corresponding to Enf denaturation and the amorphous nature of soy lecithin, respectively. Trehalose exhibited three distinct peaks corresponding to the melting peak of dihydrate and anhydrous trehalose at 102.4 and 120.8 °C, respectively, while the peak at 214.9 °C could be for the β-form of anhydrous trehalose as reported previously.[40] The absence of characteristic peaks of individual components of PLN except trehalose indicated an amorphous state of components in PLN.[41,42]

FTIR spectra of lyophilized Efa−Enf Co-loaded PLN (Figure S2b) and the physical mixture of Efa−Enf PLN components depicted −OH stretch at 3851 and 3741 cm⁻¹, similar to PLGA, Cremophor HS-15, stearic acid, Enf, and Efa. The peak at 2922 and 2852 cm⁻¹ corresponds to −CH and −CH₂ stretching, respectively. The peak at 2361 cm⁻¹ corresponds to −C≡O stretch as present in stearic acid, PLGA, and Cremophor HS-15. The peak at 1744 cm⁻¹ corresponds to the presence of ester as depicted in PLGA. The peak at 1653 and 1461 cm⁻¹ corresponds to the dihydrated form of trehalose.[43] A slight shift was observed in IR fingerprint region peaks compared to the corresponding excipients. However, the absence of any extra peak confirmed no interaction between the ingredients utilized for the preparation of PLN.[21]

3.3. CD Analysis. CD is most widely used to study the secondary structure of proteins and peptides, wherein every conformation of the protein, namely, α-helix, β-sheet, and random coiling leads to unique CD spectra. In the far-UV region (190−230 nm), the amide secondary conformation of the protein and peptide absorbs circularly polarized light to a different extent. The CD spectra of the α-helix lead to two minima at 208 nm ($\pi−\pi^*$) and 222 nm (n−π^*), while it exhibits a maxima at 191−193 nm ($\pi−\pi^*$). CD spectra of Enf and Efa−Enf Co-loaded PLN are shown in Figure 2b. They confirmed the presence of the α-helix form of Enf after encapsulation into nanoparticles; however, a red shift was observed in the spectra of Efa−Enf Co-loaded PLN, which could be due to the interaction of Enf with PLN.[44] The α-helix of Enf is essential for the insertion of Enf into the viral membrane to prevent viral fusion with cell membranes. The results indicated that the encapsulation of Enf in PLN did not affect the secondary structure of the peptide, thereby confirming the maintenance of the antiviral activity of the peptide.

3.4. Lyophilization Studies. The impact of lactose, sucrose, mannitol, and trehalose on the physical stability of the PLN during lyophilization was evaluated by freeze−thaw studies. The ratio of the final particle size after thawing to the initial particle size before freezing of the PLN nanodispersion (S_f/S_i) was calculated (Figure S2c). It has been reported that an S_f/S_i ratio <1.3 indicates good colloidal stability of nanoparticles. The characteristic features of trehalose including the selective ability to reduce the dynamics of water, higher glass-transition temperature, and absence of internal hydrogen bond enhance its ability to bind a higher number of water molecules, thus making segregation of the nanodispersion
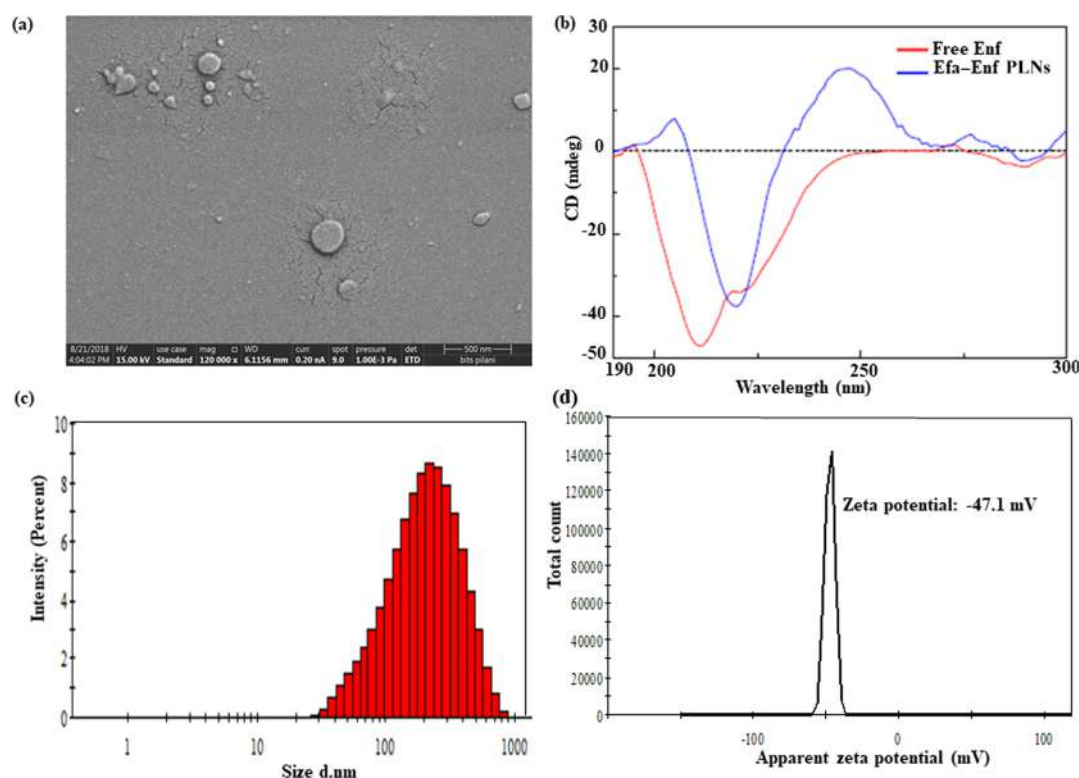
Figure 2. *In vitro* characterization of Efa−Enf PLN. (a) SEM image, (b) CD spectra of free Enf and lyophilized Efa−Enf Co-loaded PLN, (c) particle size, and (d) zeta potential of optimized Efa−Enf PLN.

evitable.[45] Therefore, trehalose was utilized for the lyophilization of Efa−Enf Co-loaded PLN. Lyophilized Efa−Enf Co-loaded PLN appeared as an amorphous and bulky powder. It revealed an S_f/S_i ratio of 1.1 ± 0.09 with Efa and Enf contents of 39.1 ± 5.23 and 0.2 ± 0.02 $\mu g/mg$, respectively.

3.5. In Vitro Drug Release Studies. The rate and extent of the drug available at the site of action depend upon the rate of drug release from the nanoformulation of cART. Therefore, a sustained release of the drugs from the nanoparticles is desirable to maintain the therapeutic drug level for weeks/months at the target site. Efa−Enf Co-loaded PLN revealed a sustained release of Efa and Enf in phosphate buffer solution (pH 7.4) at 37 °C. Free Efa ($15.2 \pm 3.36\%$) and free Enf ($79.4 \pm 2.26\%$) were released at the end of 30 min. While, 8.1 ± 1.30 and $83.4 \pm 3.70\%$ of Efa and Enf were released from PLN, respectively, in 24 h, confirming the sustained release potential of PLN (Figure S2d). The MEC required to elicit the anti-HIV effect of Enf (3.8 $\mu g/mL$)[46] is 4-fold higher than that of Efa (<1 $\mu g/mL$),[47] which is well reflected in the release profile of Efa and Enf from PLN, wherein the drug release at every time point of Enf is 5.0−10.2-fold higher than that of Efa. Also, Enf has a higher EC_{50} value (6−91 nM)[48] compared to Efa (EC_{50}—2 nM) and acts by inhibiting the first step of the viral infection which involves the restraining fusion of HIV and the host cell membrane;[49] therefore, a higher drug release of Enf compared to Efa would lead to the presentation of the drug combination in a desired fashion to the viral cell. Thus, a differential drug release of Efa and Enf might lead to synergistic killing of HIV.[50] Similar reports have been established for hydrophilic tenofovir with only 10% of the dose available for lymphatic uptake, and 90% in the free form was detectable in plasma up to 336 h with the initial peak 1 h post administration.[11] Thus, it can be contemplated that Enf

released (83%) within 24 h would pass into the blood circulation because of the permissible smaller fenestration of blood capillaries from SC spaces. However, 17% of Enf present into PLN may enter the lymphatic vessel and get trapped into the lymphocytes of the lymph node sinuses, thereby creating a depot, causing the slow release of Enf and maintaining the therapeutic concentration for a longer duration. However, an *in vivo* proof of concept is yet to be established to confirm the significance of the above differential drug release.

3.6. In Vitro Hemolysis and Blood Compatibility Studies. Depending on the size and composition, nanoparticles could exert hemolysis after reaching into the systemic circulation. Therefore, the assessment of the hemolytic potential of nanoformulations is desirable (Figure 3a,b). Blank PLN showed a non-hemolytic potential (<2%) to a slightly hemolytic potential (2−5%) as per ASTM acceptable limits. At lower concentrations, the difference in percentage hemolysis of blank and drug loaded PLN was not significant. Although, at higher concentration, hemolysis increased to $7.7 \pm 0.11\%$ compared to $4.7 \pm 1.00\%$ of blank PLN (Figure 3b). However, the percentage hemolysis of blank and drug-loaded PLN depicted a poor hemolytic potential of PLN (<10%) over the entire concentration range.[51] Further, SEM images of RBCs after treatment with blank and Efa−Enf PLN did not cause morphological changes in RBCs (Figure 3a). RBC indices and anemia are precursors for HIV-1-associated neurocognitive disorders.[52] Furthermore, the ageing of RBCs and their disposition in the spleen are portent by spicules formed on the cell surface (echinocytes).[53,54] Thus, the absence of morphological changes in RBCs is a prerequisite in HIV. The SEM image of RBCs treated with Efa−Enf Co-loaded PLN, blank PLN, and normal saline (negative control) portrayed a healthy biconcave-shaped RBC morphology, while
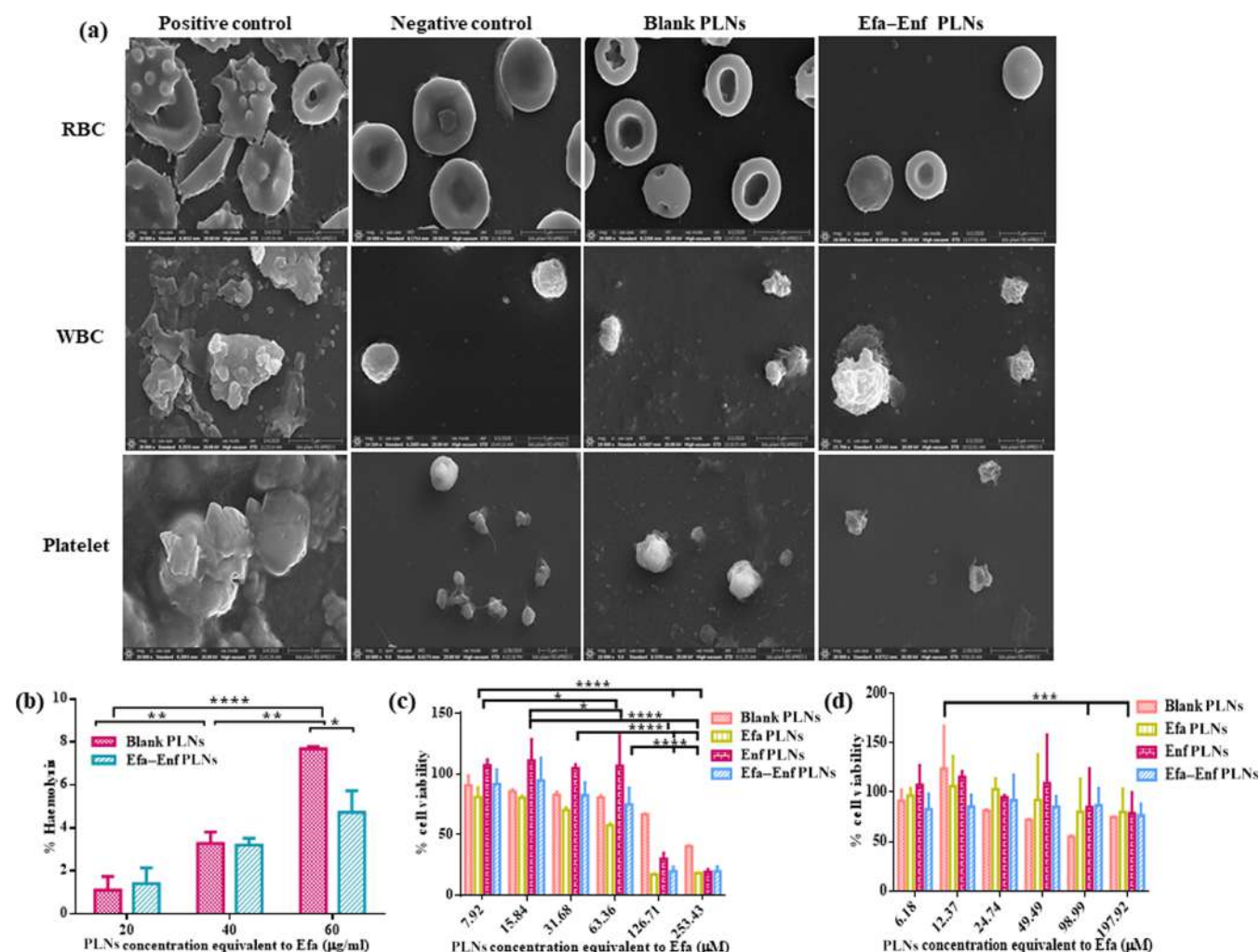
Figure 3. Hemolysis, blood compatibility, and cytotoxicity studies. (a) Scanning electron micrographs depicting the morphology of RBCs, platelets, and WBCs on treatment with blank PLN and Efa−Enf PLN, (b) percentage hemolysis of blank and Efa−Enf Co-loaded PLN, (c) WST-1 cytotoxicity studies in Jurkat E6.1 T-cells, and (d) MTT cytotoxicity studies in U937 macrophage cells. Each data represents the mean $\pm$ SD; $n = 3$; * represents $p < 0.05$, ** represents $p < 0.001$, and **** represents $p < 0.0001$ for two-way ANOVA, followed by Tukey's multiple comparison test.

positive control images revealed an irregular morphology with pore formation and echinocytes.

Further, the surface characteristic of nanoparticles may also lead to the initiation of an inflammatory response, leading to platelet aggregation and thrombosis. Therefore, platelets and WBCs of rat blood were treated with Efa−Enf PLN equivalent to 40 and 60 μg of Efa and 0.785 and 0.942 μg of Enf. Agglutinated and aggregated WBCs and platelets were observed in PEI-treated cells (positive control) (Figure 3a). However, PLN-treated cells were equivalent to normal saline-treated cells, confirming the compatibility of PLN with platelets and WBCs.

3.7. Cytotoxicity and Cell Uptake Studies. Recrudescence of the HIV-1 infection occurs because of latently infected viral sanctuaries in immune cells including macrophages and T-lymphocytes.[55] The development of LA ARV nanoformulations led to a secondary depot into these sanctuaries.[11,56] Moreover, T-cells are prone to the cytopathic effect of HIV-1 unlike macrophages.[57] Thus, cytotoxicity of LA ARV nanoformulations should be studied to avoid catastrophes in immunocompromised individuals. An insignificant difference in percentage cell viability of Jurkat E6.1 T-cells and

U937 cells was observed among blank PLN, Efa PLN, Enf PLN, and Efa−Enf PLN ($p > 0.05$) (Figure 3c,d). The cell viability was >50% for PLN equivalent to 7.92−63.36 and 6.18−197.92 μM Efa when tested in Jurkat E6.1 T-cells and U937 cells, respectively (Figure 3c,d). The reported EC_{50} values for Efa and Enf were found to be 10 and 20 nM, respectively, against HIV-1-infected macrophages as per US federal drug administration.[55] However, the cell viability of Efa−Enf PLN was >75% in U937 macrophage cells at significantly higher concentrations than their established EC_{50} value.

The cellular uptake of PLN was studied by flow cytometry (Figure 4a,b) and fluorescence microscopy (Figure 4c,d) in Jurkat E6.1 T-cells and U 937 macrophage-like cells by replacing Efa and Enf with coumarin-6. The uptake of coumarin-6-loaded PLN was significantly higher ($p < 0.0001$) than that of free coumarin-6 at 1 and 4 h in both Jurkat E6.1 T-cells and U937 cells. Coumarin-6 PLN exhibited 7.5- and 3.8-fold enhanced uptake in Jurkat E6.1 T-cells at 1 and 4 h, respectively, as compared to free coumarin-6 (Figure 4a). However, 3.5- and 3.9-fold increased coumarin-6 PLN uptake were observed compared with free coumarin-6 at 1 and
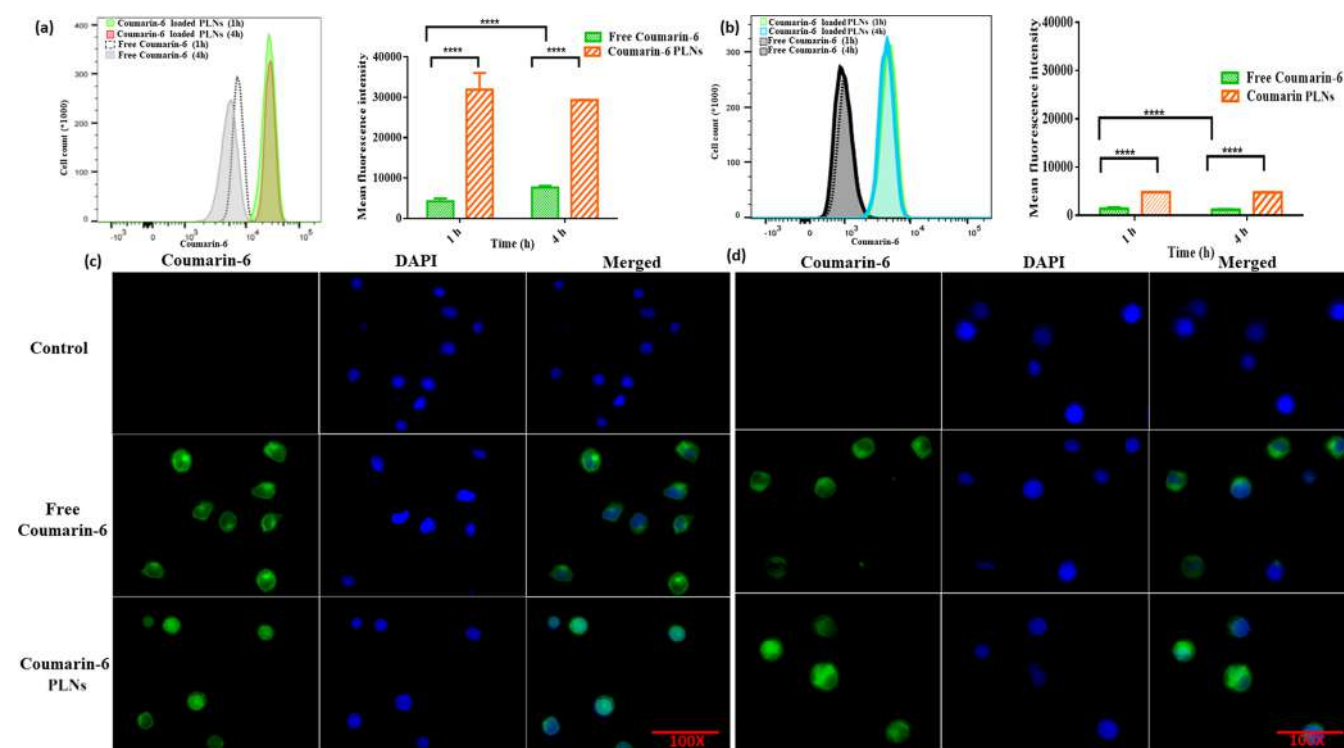
Figure 4. Cell uptake studies. (a) Histogram and quantitative time-dependent cellular uptake of free coumarin-6 and coumarin-6 PLN in Jurkat E6.1 T-cells. (b) Histogram and quantitative time-dependent cellular uptake of free coumarin-6 and coumarin-6 PLN in U937 macrophage-like cells. (c–d) Fluorescence micrographs of Jurkat E6.1 T-cells and U937 macrophage cells, respectively, after treatment with free coumarin-6 and coumarin-6 PLN and counterstaining with DAPI at 1 h. Data are expressed as the mean ± SD; **** indicates $p < 0.0001$ with a 95% confidence interval for two-way ANOVA, followed by Tukey's multiple comparison test.

4 h, respectively, in U937 macrophage-like cells (Figure 4b). However, the cellular internalization at 1 and 4 h was constant ($p > 0.05$) for free coumarin-6 and coumarin-6 PLN in both the cell suspensions. Interestingly, the cellular uptake of coumarin-6 PLN was significantly higher in difficult-to-target Jurkat E6.1 T-cells compared with U937 macrophage cells at both 1 and 4 h, respectively ($p < 0.0001$), as against free coumarin-6, which showed significantly higher uptake in Jurkat E6.1 T-cells only at 4 h ($p = 0.0004$). The enhanced T-cell uptake of coumarin-6 PLN could be attributed to the particle size-independent lipid trafficking pathway. Moreover, T-cells consist of cholesterol-dependent glycolipid invaginations responsible for hydrophobic lipid and protein trafficking.[58] Also, many viruses consist of plasma membrane-derived lipid coating and enter the uninfected T-lymphocytes by membrane fusion.[59] Moreover, the particle size (>200 nm) along with the hydrophobic surface could have contributed to intracellular delivery in macrophage cells. The fluorescence microscopy study revealed the uptake of coumarin-6 PLN in Jurkat E6.1 T-cells and U937 macrophage cells (Figure 4c,d).

3.8. *In Vivo* Biodistribution. An immune cell secondary depot has been established for LA ARV nanoformulations upon parenteral administration. For instance, intravenous (IV) infusion of the ibalizumab monoclonal antibody (2000 mg loading dose, followed by 800 mg maintenance dose every 14 days) leads to CD4 T-cell receptor occupancy up to 25 weeks.[60] Therefore, DiR PLN (Efa−Enf Co-loaded PLN surrogate) upon IV administration might have led to the omnivorous immune cell depot which was carried to various organs preceding distribution to the liver as depicted by the higher accumulation in the liver compared with other organs

[1, 2, 4, 8, 10, and 24 h and the initiation of non-uniform biodistribution throughout the body within 2 h post administration and leading to the tissue-specific immune cell depot (Figure 5a)]. Infected blood monocytes and Kupffer cells (differentiated macrophages) of the liver consist of HIV-1 proviral DNA.[61] Further, Kupffer cells harbor more HIV-1 strain than hepatocytes.[62] Therefore, delivery of nanoparticles to macrophages lining the liver with the subsequent release into the T-lymphocyte residence site is desirable for HIV treatment.[63] Each animal in group I was sacrificed after 24 h, and the fluorescence intensity in HIV infection-associated organs was determined to quantify the uptake of DiR PLN (Figure S3). The accumulation of surrogate DiR PLN in different organs was observed in the order of spleen ≥ liver > lymph node > thymus > lungs > FRT > heart > kidneys > brain after IV administration (Figure 5c). The availability of PLN to various tissue parenchyma credence upon modulation in the nanoparticle size, wherein larger particles are phagocytosed by macrophagic cells including Kupffer cells (>200 nm)[64] and dendritic cells (>500 nm) in lymph nodes.[65] The average particle size of DiR PLN was 212.5 ± 31.79 nm, making particles <200 nm available to parenchymal cells of the liver, spleen, and lymph nodes. Higher biodistribution of DiR PLN in the spleen (15% T-lymphocytes) and lymph nodes (75% T-lymphocytes) among other organs harboring latently infected T-lymphocytes was achieved. However, the fluorescence intensity was 4-fold higher in the spleen (HIV reservoir site) than in the lymph node and thymus.

The route of administration augments the LA potential of the administered nanoformulation because of the primary (injection site) and secondary (infiltered immune cells) depot
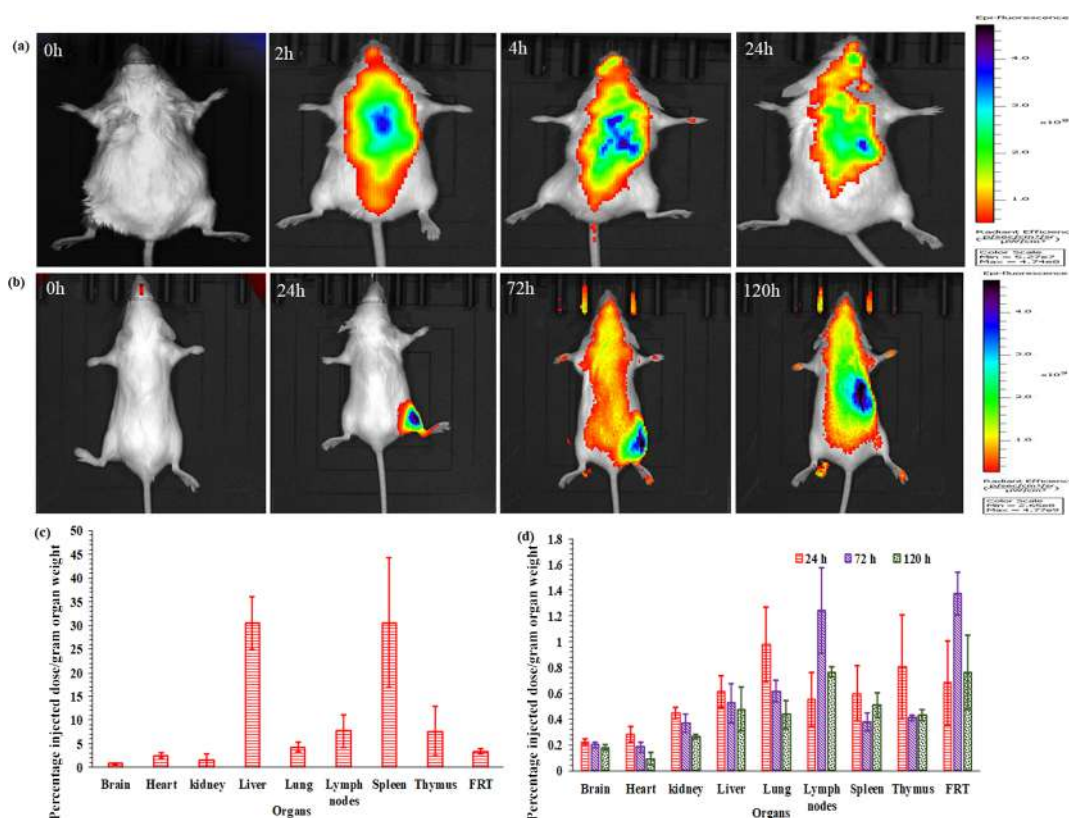
Figure 5. *In vivo* biodistribution studies. (a) Whole-body image after IV administration of DiR PLN at 0, 2, 4, and 24 h. (b) Whole-body image after SC administration of DiR PLN at 0, 24, 72, and 120 h. (c) Biodistribution of DiR PLN in different organs after IV administration in 24 h. (d) Biodistribution of DiR PLN in different organs after SC administration in 24, 72, and 120 h. Data are represented as the mean $\pm$ SD, n = 3.

genesis.[9] To this end, biodistribution studies of DiR PLN were assessed by SC administration. Only $13.3 \pm 0.76\%$ of the injected dose was biodistributed in reticuloendothelial system (RES) and non-RES organs after 5 days as against $88.7 \pm 19.34\%$ injected dose biodistributed to the whole body within 24 h when administered intravenously. Furthermore, the primary depot was evident even at day 5 upon SC administration (Figure 5b), highlighting the LA potential of the developed PLN. The slow effective release of DiR PLN was confirmed by non-uniform biodistribution at day 3 post administration. The images of organs obtained after sacrificing animals of groups II, III, and IV at days 1, 3, and 5 post SC administration are shown in Figure S3. Higher administration of DiR PLN in the lymph node (containing 75% T-lymphocytes) was obtained compared to the spleen in contrast to IV administration at day 3 post administration. Sequestration of DiR PLN in the lymph node was the aftermath of lymphatic uptake post SC administration, where from the PLN would slowly be transported to the thoracic duct and loaded into the systemic circulation. Similar observations were previously reported for combination drug nanoparticles of lopinavir, ritonavir, and tenofovir producing three waves in plasma corresponding to fast (<8 h), intermediate (8−24 h), and protracted (>48 h to 2 weeks) drug release through the lymphatic-circulatory conjoint.[11] It was observed that DiR PLN were accumulated and retained in the infection-spread site (lymph nodes) and reservoir sites (liver and spleen) after SC administration with a total percentage injected dose/gram organ weight of 2.56, 2.25, and 1.99% after days 1, 3, and 5, respectively (Figure 5d). Previously, LA slow-release rilpivirine nanocrystals were also localized in the liver, spleen, popliteal,

and axillary lymph node after SC administration.[66] The biodistribution of DiR PLN was also observed in difficult-to-access locations including the brain because of carriage by secondary depot cells, wherein the percentage injected dose of DiR PLN/gram organ weight was found to be 0.22, 0.19, and 0.18% at days 1, 3, and 5, respectively, post SC dosing. The tissue concentration of DiR PLN in the brain depicted no significant change until 5 days, emphasizing the role of the secondary depot forming monocytes which are customary to traverse through a privileged organ such as the brain.[67,68] Therefore, enhanced lymphatic and brain uptake of DiR PLN would lead to the possible elimination of HIV relapse.

The percentage injected dose/gram organ weight at the HIV infection site (FRT) was found to be 0.67, 1.37, and 0.76% at the 1st, 3rd, and 5th day, respectively, post SC dosing, suggesting wider potential in pre-exposure prophylaxis with an increase in PLN uptake up to the 3rd day ($1.3 \pm 0.16\%$) at the HIV infection site. Similar observations were reported previously for an LA slow-release nanoformulation loaded with tenofovir alafenamide and elvitegravir with great potential in pre-exposure prophylaxis, wherein a 1.65-fold higher concentration of drug-loaded nanoparticles in the FRT was obtained compared to the free drug and a sustained release up to 336 h.[69] No significant difference ($p > 0.05$) was observed in the fluorescence intensity at day 1 (group II), day 3 (group III), and day 5 (group IV) in each organ including RES organs, kidneys, heart, FRT, and brain, underpinning the LA slow drug delivery potential of PLN. Nevertheless, the quantification of drugs in every organ is required to confirm that the minimum effective concentration of drugs has been achieved.
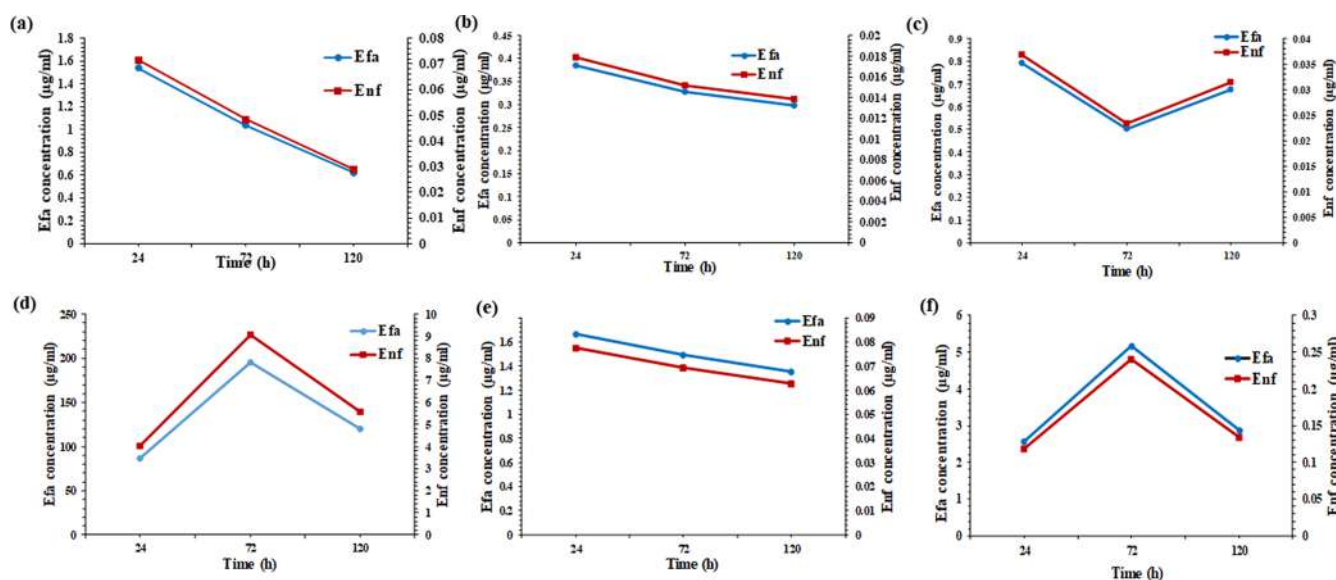
Figure 6. Simulated Efa and Enf concentrations in different organs. (a) Draining organs (heart, lungs, and kidneys), (b) liver, (c) spleen, (d) lymph node, (e) brain, and (f) FRT.

3.9. Prediction of the Dose and Target Site Drug Level by Simulation of the DiR PLN Biodistribution Profile.

It is essential to attain the minimum effective drug concentration at the infection sites (e.g., the spleen, lymph nodes, brain, and FRT) for complete eradication of the virus from the body. Infrared dye (e.g., DiR)-loaded nanoparticles are most widely used as a surrogate to establish the biodistribution pattern of nanoparticles by bioimaging of live animals. However, this sophisticated high-throughput technique does not provide the actual available tissue level of the drugs which is necessary to define the drug concentration at the injection site.

In the present study, we attempted to predict the available drug levels at target sites by simulation of the DiR PLN biodistribution profile. The model predicted a significantly higher concentration of both Efa and Enf in the lymph node upon SC administration. A higher amount of sequestered PLN in macrophages and T-lymphocytes of the lymph node might have led to a slow effective release into the lymphatic vesicles, thereby draining into the thoracic duct and presenting into the systemic circulation. Once the secondary immune cell depot is into the systemic circulation, it causes a protracted drug release after differentiating into various tissues depending upon the differential blood flow volume to each organ.[11,56] Furthermore, the order of predicted available tissue concentration is FRT > brain > draining organ > spleen > liver. The predicted higher amounts of available Efa and Enf in the FRT (the major infection site) and brain (the most inaccessible organ) could be attributed to the higher-blood-volume-containing secondary depot to these organs. Furthermore, the predicted available tissue concentration of Efa (an EC_{50} of 2 nM) and Enf (an EC_{50} of 6–91 nM) was found to be higher than the effective concentration in all the organs (Figure 6) until day 5 for an administered dose of PLN equivalent to 1250 and 58.17 μg of Efa and Enf, respectively. Nevertheless, preclinical studies have yet to be performed to establish the accurate tissue concentration and efficacy of the formulation.

4. CONCLUSIONS

The current study is the first proof of concept of LA potential for novel cART, namely, Efa and Enf, when loaded into PLN. Furthermore, Efa–Enf PLN depicted enhanced intracellular delivery to established secondary depot and hub for the transcriptionally dormant form of HIV-1, which include macrophages and T-cells. Additionally, it highlights the implication of SC administration for a week-long protracted drug release through the secondary depot in systemic circulation preceded *via* the lymphatic route, which could be well corroborated with the *in vitro* drug release of Efa and Enf from PLN. The distinctive LA contrivance of surrogate PLN caused sustained delivery to the major infection-spread and reservoir sites. Furthermore, blood flow to a specific organ inflects the biodistribution of PLN available in the secondary depot. To this end, correlation studies have been performed as the first illustration to estimate the dose of Efa–Enf PLN desirable for establishing the required tissue concentration of Efa and Enf in each organ, which would be lucrative in preserving time and cost during preclinical studies.

■ ASSOCIATED CONTENT

Ⓢ Supporting Information

The Supporting Information is available free of charge at https://pubs.acs.org/doi/10.1021/acs.molpharmaceut.0c00773.

Perturbation plots obtained during optimization of Efa–Enf PLN, *in vitro* characterization studies of Efa–Enf PLN, organ images of sacrificed animals administered with DiR-loaded PLN *via* the IV and SC routes, experimental runs, ANOVA results obtained by Box–Behnken design, and details of surrogate PLN (PDF)

■ AUTHOR INFORMATION

Corresponding Authors

Anil B. Jindal − *Department of Pharmacy, Birla Institute of Technology and Science Pilani, Jhunjhunu, Rajasthan 333031, India;* ⓞ orcid.org/0000-0003-3856-869X; Phone: +911596 51 5602

Vikas D. Dighe − *National Centre for Preclinical Reproductive and Genetic Toxicology ICMR, National Institute for Research in Reproductive Health, Mumbai, Maharashtra 400012, India;* Phone: +912224192139; Email: dighev@nirrh.res.in, dighevikas@hotmail.com

Authors

Dhanashree H. Surve − *Department of Pharmacy, Birla Institute of Technology and Science Pilani, Jhunjhunu, Rajasthan 333031, India*

Yugandhara B. Jirwankar − *National Centre for Preclinical Reproductive and Genetic Toxicology ICMR, National Institute for Research in Reproductive Health, Mumbai, Maharashtra 400012, India*

Complete contact information is available at:
https://pubs.acs.org/10.1021/acs.molpharmaceut.0c00773

Notes

The authors declare no competing financial interest.

■ ABBREVIATIONS

cART, combination antiretroviral therapy; CD, circular dichroism; DiR, 1,1′-dioctadecyl-3,3,3′,3′-tetramethylindotri-carbocyanine iodide; % EE, percentage entrapment efficiency; Efa, Efavirenz; Enf, Enfuvirtide (T-20); FACS, fluorescence-activated cell sorting; HAART, highly active antiretroviral therapy; LA, long-acting; PDI, polydispersity index; PLN, polymer−lipid hybrid nanoparticles; PLGA, poly(lactic-*co*-glycolic acid); SD, standard deviation; OD, optical density

■ REFERENCES

(1) Smit, M.; Smit, C.; Geerlings, S.; Gras, L.; Brinkman, K.; Hallett, T. B.; de Wolf, F. Changes in First-Line CART Regimens and Short-Term Clinical Outcome between 1996 and 2010 in The Netherlands. *PLoS One* **2013**, *8*, e76071.

(2) Delaney, M. History of HAART − the True Story of How Effective Multi-Drug Therapy Was Developed for Treatment of HIV Disease. *Retrovirology* **2006**, *3*, S6.

(3) Sosnik, A.; Augustine, R. Challenges in Oral Drug Delivery of Antiretrovirals and the Innovative Strategies to Overcome Them. *Adv. Drug Delivery Rev.* **2016**, *103*, 105−120.

(4) Nachega, J. B.; Marconi, V. C.; van Zyl, G. U.; Gardner, E. M.; Preiser, W.; Hong, S. Y.; Mills, E. J.; Gross, R. HIV Treatment Adherence, Drug Resistance, Virologic Failure: Evolving Concepts. *Infect. Disord. - Drug Targets* **2011**, *11*, 167−174.

(5) Roser, M.; Hannah, R. HIV/AIDS. https://ourworldindata.org/hiv-aids (accessed Apr 17, 2020).

(6) Aungst, B. J. P-Glycoprotein, Secretory Transport, and Other Barriers to the Oral Delivery of Anti-HIV Drugs. *Adv. Drug Delivery Rev.* **1999**, *39*, 105−116.

(7) Edagwa, B.; Zhou, T.; JoE, M.; Liu, X.-M.; Gendelman, H. Development of HIV Reservoir Targeted Long Acting Nano-formulated Antiretroviral Therapies. *Curr. Med. Chem.* **2014**, *21*, 4186−4198.

(8) Owen, A.; Rannard, S. Strengths, Weaknesses, Opportunities and Challenges for Long Acting Injectable Therapies: Insights for Applications in HIV Therapy. *Adv. Drug Delivery Rev.* **2016**, *103*, 144−156.

(9) Surve, D. H.; Jindal, A. B. Recent Advances in Long-Acting Nanoformulations for Delivery of Antiretroviral Drugs. *J. Controlled Release* **2020**, *324*, 379−404.

(10) Zhou, T.; Su, H.; Dash, P.; Lin, Z.; Shetty, B. L. D.; Kocher, T.; Szlachetka, A.; Lamberty, B.; Fox, H. S.; Poluektova, L.; et al. Creation of a Nanoformulated Cabotegravir Prodrug with Improved Anti-retroviral Profiles. *Biomaterials* **2018**, *151*, 53−65.

(11) Kraft, J. C.; McConnachie, L. A.; Koehn, J.; Kinman, L.; Sun, J.; Collier, A. C.; Collins, C.; Shen, D. D.; Ho, R. J. Y. Mechanism-Based Pharmacokinetic (MBPK) Models Describe the Complex Plasma Kinetics of Three Antiretrovirals Delivered by a Long-Acting Anti-HIV Drug Combination Nanoparticle Formulation. *J. Controlled Release* **2018**, *275*, 229−241.

(12) Janssen Announces Health Canada Approval of CABENU-VATM, the First Long-Acting Regimen for the Treatment of HIV. https://www.jnj.com/janssen-announces-health-canada-approval-of-cabenuva-the-first-long-acting-regimen-for-the-treatment-of-hiv (accessed May 11, 2020).

(13) Margolis, D. A.; Gonzalez-garcia, J.; Stellbrink, H.; Eron, J. J.; Yazdanpanah, Y.; Podzamczer, D.; Lutz, T.; Angel, J. B.; Richmond, G. J.; Clotet, B.; et al. Long-Acting Intramuscular Cabotegravir and Rilpivirine in Adults with HIV-1 Infection (LATTE-2): 96-Week Results of a Randomised , Open-Label , Phase 2b , Non-Inferiority Trial. *Lancet* **2017**, *390*, 1499−1510.

(14) Mandal, S.; Prathipati, P. K.; Kang, G.; Zhao, Y.; Yuan, Z.; Fan, W.; Li, Q.; Destache, C. Tenofovir Alafenamide and Elvitegravir Loaded Nanoparticles for Long-Acting Prevention of HIV-1 Vaginal Transmission. *AIDS* **2017**, *31*, 469−476.

(15) Mandal, S.; Kang, G.; Prathipati, P. K.; Zhou, Y.; Fan, W.; Li, Q.; Destache, C. J. Nanoencapsulation Introduces Long-Acting Phenomenon to Tenofovir Alafenamide and Emtricitabine Drug Combination : A Comparative Pre- Exposure Prophylaxis e Fficacy Study against HIV-1 Vaginal Transmission. *J. Controlled Release* **2019**, *294*, 216−225.

(16) Mandal, S.; Belshan, M.; Holec, A.; Zhou, Y.; Destache, C. An Enhanced Emtricitabine-Loaded Long-Acting Nanoformulation for Prevention or Treatment of HIV Infection. *Antimicrob. Agents Chemother.* **2017**, *61* 1−11.

(17) Freeling, J. P.; Koehn, J.; Shu, C.; Sun, J.; Ho, R. J. Y. Anti-HIV Drug-Combination Nanoparticles Enhance as Well as Triple-Drug Combination Levels in Cells Within Lymph Nodes and Blood in Primates. *AIDS Res. Hum. Retrovir.* **2015**, *31*, 107−114.

(18) Duan, J.; Freeling, J. P.; Koehn, J.; Shu, C.; Ho, R. J. Y. Evaluation of Atazanavir and Darunavir Interactions with Lipids for Developing PH-Responsive Anti-HIV Drug Combination Nano-particles. *J. Pharm. Sci.* **2014**, *103*, 2520−2529.

(19) Freeling, J. P.; Koehn, J.; Shu, C.; Sun, J.; Ho, R. J. Y. Long-Acting Three-Drug Combination Anti-HIV Nanoparticles Enhance Drug Exposure in Primate Plasma and Cells within Lymph Nodes and Blood. *AIDS* **2014**, *28*, 2625−2631.

(20) Best, B. M.; Goicoechea, M. Efavirenz-Still First Line King? *Expert Opin. Drug Metab. Toxicol.* **2008**, *4*, 965−972.

(21) Raina, H.; Kaur, S.; Jindal, A. B. Development of Efavirenz Loaded Solid Lipid Nanoparticles: Risk Assessment, Quality-by-Design (QbD) Based Optimisation and Physicochemical Character-isation. *J. Drug Delivery Sci. Technol.* **2017**, *39*, 180−191.

(22) Makwana, V.; Jain, R.; Patel, K.; Nivsarkar, M.; Joshi, A. Solid Lipid Nanoparticles (SLN) of Efavirenz as Lymph Targeting Drug Delivery System: Elucidation of Mechanism of Uptake Using Chylomicron Flow Blocking Approach. *Int. J. Pharm.* **2015**, *495*, 439−446.

(23) Labonte, J.; Lebbos, J.; Kirkpatrick, P. Enfuvirtide. *Nat. Rev. Drug Discovery* **2003**, *2*, 345−346.

(24) Vernazza, P. L.; Schmid, P. *Antiviral Drugs*; Elsevier B.V., 2005; Vol. 28.

(25) Hardy, H.; Skolnik, P. R. Enfuvirtide a New Fusion Inhibitor for Therapy of Human Immunodeficiency Virus Infection. *Pharmacotherapy* **2004**, *24*, 198−211.

(26) Patel, I. H.; Zhang, X.; Nieforth, K.; Salgo, M.; Buss, N. Pharmacokinetics, Pharmacodynamics and Drug Interaction Potential of Enfuvirtide. *Clin. Pharmacokinet.* **2005**, *44*, 175−186.

(27) Li, W.; Yu, F.; Wang, Q.; Qi, Q.; Su, S.; Xie, L.; Lu, L.; Jiang, S. Co-Delivery of HIV-1 Entry Inhibitor and NNRTI Shuttled by Nanoparticles: Cocktail Therapeutics Strategy for Antiviral Therapy. *AIDS* **2016**, *30*, 827−838.

(28) Gallarate, M.; Trotta, M.; Battaglia, L.; Chirio, D. Preparation of Solid Lipid Nanoparticles from W/O/W Emulsions: Preliminary Studies on Insulin Encapsulation. *J. Microencapsul.* **2009**, *26*, 394−402.

(29) Surve, D. H.; Jindal, A. B. Development and Validation of Reverse-Phase High-Performance Liquid Chromatographic (RP-HPLC) Method for Quantification of Efavirenz in Efavirenz-Enfuvirtide Co-Loaded Polymer-Lipid Hybrid Nanoparticles. *J. Pharm. Biomed. Anal.* **2019**, *175*, 112765.

(30) Joshy, K. S.; Snigdha, S.; Kalarikkal, N.; Pothen, L. A.; Thomas, S. *Gelatin Modified Lipid Nanoparticles for Anti Retroviral Drug Delivery*; Elsevier Ireland Ltd., 2017.

(31) Chen, G.; Wen, J. Poly(Lactic-Co-Glycolic Acid) Based Double Emulsion Nanoparticle as a Carrier System to Deliver Glutathione Sublingually. *Biomed. J.* **2018**, *3*, 50−59.

(32) Gryparis, E. C.; Mattheolabakis, G.; Bikiaris, D.; Avgoustakis, K. Effect of Conditions of Preparation on the Size and Encapsulation Properties of PLGA-MPEG Nanoparticles of Cisplatin. *Drug Delivery* **2007**, *14*, 371−380.

(33) Cooper, D. L.; Harirforoosh, S. Effect of Formulation Variables on Preparation of Celecoxib Loaded Polylactide-Co-Glycolide Nanoparticles. *PLoS One* **2014**, *9*, e113558.

(34) Hao, J.; Fang, X.; Zhou, Y.; Wang, J.; Guo, F.; Li, F.; Peng, X. Development and Optimization of Solid Lipid Nanoparticle Formulation for Ophthalmic Delivery of Chloramphenicol Using a Box-Behnken Design. *Int. J. Nanomed.* **2011**, *6*, 683−692.

(35) Pradhan, S.; Hedberg, J.; Blomberg, E.; Wold, S.; Wallinder, I. O. Effect of Sonication on Particle Dispersion, Administered Dose and Metal Release of Non-Functionalized, Non-Inert Metal Nanoparticles. *J. Nanoparticle Res.* **2016**, *18*, 285.

(36) Cun, D.; Jensen, D. K.; Maltesen, M. J.; Bunker, M.; Whiteside, P.; Scurr, D.; Foged, C.; Nielsen, H. M. High Loading Efficiency and Sustained Release of SiRNA Encapsulated in PLGA Nanoparticles: Quality by Design Optimization and Characterization. *Eur. J. Pharm. Biopharm.* **2011**, *77*, 26−35.

(37) Kruger, F. W. H.; McGill, W. J. A DSC Study of Curative Interactions. I. The interaction of ZnO, sulfur, and stearic acid. *J. Appl. Polym. Sci.* **1991**, *42*, 2643−2649.

(38) Passerini, N.; Craig, D. Q. M. An Investigation into the Effects of Residual Water on the Glass Transition Temperature of Polylactide Microspheres Using Modulated Temperature DSC. *J. Contr. Release* **2001**, *73*, 111−115.

(39) Liu, L.; Mao, K.; Wang, W.; Pan, H.; Wang, F.; Yang, M.; Liu, H. Kolliphor HS 15 Micelles for the Delivery of Coenzyme Q10 : Preparation , Characterization , and Stability. *AAPS PharmSciTech* **2016**, *17*, 757−766.

(40) Verhoeven, N.; Neoh, T. L.; Furuta, T.; Yamamoto, C.; Ohashi, T.; Yoshii, H. Characteristics of Dehydration Kinetics of Dihydrate Trehalose to Its Anhydrous Form in Ethanol by DSC. *Food Chem.* **2012**, *132*, 1638−1643.

(41) Ding, Y.; Nielsen, K. A.; Nielsen, B. P.; Bøje, N. W.; Müller, R. H.; Pyo, S. M. Lipid-Drug-Conjugate (LDC) Solid Lipid Nanoparticles (SLN) for the Delivery of Nicotine to the Oral Cavity − Optimization of Nicotine Loading Efficiency. *Eur. J. Pharm. Biopharm.* **2018**, *128*, 10−17.

(42) Ansari, M. J.; Anwer, M. K.; Jamil, S.; Al-shdefat, R.; Ali, B. E.; Ahmad, M. M.; Ansari, M. N. Enhanced Oral Bioavailability of Insulin-Loaded Solid Lipid Nanoparticles: Pharmacokinetic Bioavail-

ability of Insulin-Loaded Solid Lipid Nanoparticles in Diabetic Rats. *Drug Delivery* **2015**, *23*, 1972−1979.

(43) Márquez, M. J.; Romani, D.; Díaz, S. B.; Brandán, S. A. Structural and Vibrational Characterization of Anhydrous and Dihydrated Species of Trehalose Based on the FTIR and FTRaman Spectra and DFT Calculations. *J. King Saud Univ. Sci.* **2018**, *30*, 229−249.

(44) Azizi, A.; Ranjbar, B.; Moghadam, T. T.; Bagheri, Z. Plasmonic Circular Dichroism Study of DNA − Gold Nanoparticles Bioconjugates. *Plasmonics* **2014**, *9*, 273−281.

(45) Te, J. A.; Tan, M.-L.; Ichiye, T. SOlvation of Glucose, Trehalose and Sucrose by the Soft Sticky Dipole-Quadrupole-OCtupole Water Model. *Chem. Phys. Lett.* **2010**, *491*, 218−223.

(46) Lindsay, G.; Crowe, S.; McCarthy, J.; Mills, K.; Mouton, J.; Norrby, R.; Paterson, D.; Pfaller, M. *The Use of Antibiotics*; Taylor & Francis Group, 2012.

(47) Huang, S.-H.; Lin, S.-W.; Chang, S.-Y.; Lin, Y.-T.; Chiang, C.; Hsiao; Sun, H.-Y.; Liu, W.-C.; Su, Y.-C.; Hung, C.-C.; Chang, S.-C. Prediction of Plasma Efavirenz Concentrations among HIV- Positive Patients Taking Efavirenz- Containing Combination Antiretroviral Therapy. *Sci. Rep.* **2017**, *7*, 16187.

(48) Cheng, S.; Wang, Y.; Zhang, Z.; Lv, X.; Gao, G. F.; Shao, Y.; Ma, L.; Li, X. Enfuvirtide ̂̌PEG Conjugate: A Potent HIV Fusion Inhibitor with Improved Pharmacokinetic Properties. *Eur. J. Med. Chem.* **2016**, *121*, 232−237.

(49) Lee, W.-G.; Frey, K. M.; Gallardo-Macias, R.; Spasov, K. A.; Bollini, M.; Anderson, K. S.; Jorgensen, W. L. Picomolar Inhibitors of HIV - 1 Reverse Transcriptase: Design and Crystallography of Naphthyl Phenyl Ethers. *ACS Med. Chem. Lett.* **2014**, *5*, 1259−1262.

(50) Morton, S. W.; Lee, M. J.; Deng, Z. J.; Dreaden, E. C.; Siouve, E.; Shopsowitz, K. E.; Shah, N. J.; Yaffe, M. B.; Hammond, P. T. A Nanoparticle-Based Combination Chemotherapy Delivery System for Enhanced Tumor Killing by Dynamic Rewiring of Signaling Pathways. *Sci. Signal.* **2014**, *7*, ra44.

(51) Burlui, V.; Popa, M.; Cadinoiu, A. N.; Stadoleanu, C.; Zamaru, V.; Dârțu, L.; Folescu, E.; Rață, D. M. Physico-Chemical Characterization and in Vitro Haemolysis Evaluation of Titanium Dioxide Nanoparticles. *Biomaterials* **2015**, *S*, 124.

(52) Kallianpur, A. R.; Wang, Q.; Jia, P.; Hulgan, T.; Zhao, Z.; Letendre, S. L.; Ellis, R. J.; Heaton, R. K.; Franklin, D. R.; Barnholtzsloan, J.; et al. Anemia and Red Blood Cell Indices Predict HIV-Associated Neurocognitive Impairment in the Highly Active Antiretroviral Therapy Era. *J. Infect. Dis.* **2016**, *213*, 1065−1073.

(53) Wong, K. H. K.; Sandlin, R. D.; Carey, T. R.; Miller, K. L.; Shank, A. T.; Oklu, R.; Maheswaran, S.; Haber, D. A.; Irimia, D.; Stott, S. L.; et al. The Role of Physical Stabilization in Whole Blood Preservation. *Sci. Rep.* **2016**, *6*, 21023.

(54) Zvetkova, E.; Fuchs, D. Medical Significance of Simultaneous Application of Red Blood Cell Distribution Width (RDW) and Neopterin as Diagnostic / Prognostic Biomarkers in Clinical Practice. *Pteridines* **2017**, *28*, 133−140.

(55) Gavegnano, C.; Schinazi, R. Antiretroviral Therapy in Macrophages: Implication for HIV Eradication. *Antivir. Chem. Chemother.* **2009**, *20*, 63−78.

(56) Zhou, T.; Su, H.; Dash, P.; Lin, Z.; Shetty, B. L. D.; Kocher, T.; Szlachetka, A.; Lamberty, B.; Fox, H. S.; Poluektova, L.; et al. Creation of a Nanoformulated Cabotegravir Prodrug with Improved Antiretroviral proFiLes. *Biomaterials* **2018**, *151*, 53−65.

(57) Kruize, Z.; Kootstra, N. A. The Role of Macrophages in HIV-1 Persistence and Pathogenesis. *Front. Microbiol.* **2019**, *10*, 2828.

(58) Surve, D.; Dandekar, P.; Devarajan, P.; Jindal, A. Intracellular Delivery: An Overview. *Targeted Intracellular Drug Delivery by Receptor Mediated Endocytosis*; Springer, 2019; pp 3−44.

(59) Majorovits, E.; Nejmeddine, M.; Tanaka, Y.; Taylor, G. P.; Fuller, S. D.; Bangham, C. R. M. Human T-Lymphotropic Virus-1 Visualized at the Virological Synapse by Electron Tomography. *PLoS One* **2008**, *3*, e2251.

(60) Beccari, M. V.; Mogle, B. T.; SIdman, E. F.; Mastro, K. A.; Reddy, E. A.; Kufel, W. D. Ibalizumab , a Novel Monoclonal Antibody

for the Management of Multidrug-Resistant HIV-1 Infection. *Antimicrob. Agents Chemother.* **2019**, *63*, e00110−e00119.

(61) Hufert, F.; Schmitz, J.; Schreiber, M.; Schmitz, H.; Rácz, P.; von Laer, D. Human Kupffer Cells Infected with HIV-1. *J. Acquir. Immune Defic. Syndr.* **1988**, *6*, 772−777.

(62) Housset, C.; Boucher, O.; Girard, P. M.; Leibowitch, J.; Saimot, A. G.; Bréchot, C.; Marche, C. Immunohistochemical Evidence for Human Lmmunodeficiency Virus-l Infection of Liver Kupffer Cells. *Hum. Pathol.* **1990**, *21*, 404−408.

(63) Jiang, L.; Wang, T.; Wang, Y.; Wang, Z.; Bai, Y. Co-Disposition of Chitosan Nanoparticles by Multi Types of Hepatic Cells and Their Subsequent Biological Elimination: The Mechanism and Kinetic Studies at the Cellular and Animal Levels. *Int. J. Nanomed.* **2019**, *14*, 6035−6060.

(64) Chow, D.; Hwang, J. Targeting Small Unilamellar Cells by Dose Effect1 Liposomes to Hepatic Parenchymal. *J. Pharmacol. Exp. Ther.* **1989**, *248*, 506−513.

(65) Chang, T. Z.; Stadmiller, S. S.; Staskevicius, E.; Champion, J. A. Effects of Ovalbumin Protein Nanoparticle Vaccine Size and Coating on Dendritic Cell Processing. *Biomater. Sci.* **2017**, *5*, 223−233.

(66) Ottemann, B. M.; Helmink, A. J.; Zhang, W.; Mukadam, I.; Woldstad, C.; Hilaire, J. R.; Liu, Y.; Mcmillan, J. M.; Edagwa, B. J.; Mosley, R. L.; et al. Bioimaging Predictors of Rilpivirine Biodistribution and Antiretroviral Activities. *Biomaterials* **2018**, *185*, 174−193.

(67) Klyachko, N. L.; Polak, R.; Haney, M. J.; Zhao, Y.; Neto, J. G.; Hill, M. C.; Kabanov, A. V.; Cohen, R. E.; Rubner, F.; Batrakova, E. V.; et al. Macrophages with Cellular Backpacks for Targeted Drug Delivery to the Brain. *Biomaterials* **2017**, *140*, 79−87.

(68) He, W.; Kapate, N.; Iv, C. W. S. Drug Delivery to Macrophages: A Review of Targeting Drugs and Drug Carriers to Macrophages for Inflammatory Diseases. *Adv. Drug Delivery Rev.* **2019**, DOI: 10.1016/j.addr.2019.12.001.

(69) Prathipati, P. K.; Mandal, S.; Pon, G.; Vivekanandan, R.; Destache, C. J. Pharmacokinetic and Tissue Distribution Profile of Long Acting Tenofovir Alafenamide and Elvitegravir Loaded Nanoparticles in Humanized Mice Model. *Pharm. Res.* **2017**, *34*, 2749−2755.